



# Numerical Analysis of Static and Dynamic Performances of Grid Fin Controlled Missiles

Antoine Despeyroux, Jean-Pierre Hickey, Robert Desaulnier,  
Ryan Luciano, and Michael Piotrowski  
Royal Military College of Canada  
Kingston, Ontario K7K 7B4

Nicolas Hamel  
Defence Research and Development Canada – Valcartier Research Centre  
Quebec City, Québec G3J 1X5

Journal of Spacecraft and Rockets  
DOI: 10.2514/1.A33189

Date of Publication from Ext Publisher: May 2015

**Defence Research and Development Canada**

**External Literature (P)**

DRDC-RDDC-2017-P134

December 2017

## CAN UNCLASSIFIED

### IMPORTANT INFORMATIVE STATEMENTS

**Disclaimer:** This document is not published by the Editorial Office of Defence Research and Development Canada, an agency of the Department of National Defence of Canada, but is to be catalogued in the Canadian Defence Information System (CANDIS), the national repository for Defence S&T documents. Her Majesty the Queen in Right of Canada (Department of National Defence) makes no representations or warranties, expressed or implied, of any kind whatsoever, and assumes no liability for the accuracy, reliability, completeness, currency or usefulness of any information, product, process or material included in this document. Nothing in this document should be interpreted as an endorsement for the specific use of any tool, technique or process examined in it. Any reliance on, or use of, any information, product, process or material included in this document is at the sole risk of the person so using it or relying on it. Canada does not assume any liability in respect of any damages or losses arising out of or in connection with the use of, or reliance on, any information, product, process or material included in this document.

This document was reviewed for Controlled Goods by Defence Research and Development Canada (DRDC) using the Schedule to the *Defence Production Act*.

# Numerical Analysis of Static and Dynamic Performances of Grid Fin Controlled Missiles

Antoine Despeyroux,<sup>\*</sup> Jean-Pierre Hickey,<sup>†</sup> Robert Desaulnier,<sup>‡</sup> Ryan Luciano,<sup>‡</sup> and Michael Piotrowski<sup>‡</sup>

Royal Military College of Canada, Kingston, Ontario K7K 7B4, Canada  
and

Nicolas Hamel<sup>§</sup>

Defence Research and Development Canada, Quebec City, Québec G3J 1X5, Canada

DOI: 10.2514/1.A33189

Grid fins provide good maneuverability to missiles in supersonic flow because they can maintain lift at a higher angle of attack. Although static aerodynamic data exist, very little quantitative dynamic performance information is available for grid fin controlled missiles. The high drag associated with grid fins is also a concern. Dynamic simulations are carried out using computational fluid dynamics to investigate the dynamic stability of a generic missile, controlled by grid fins or planar fins, in supersonic and transonic regimes at angles of attack up to 30 deg. In supersonic flow, the pitch-damping derivative is found to be insensitive to the control fin type; however, in transonic flow, grid fins provide a lower damping in pitch than planar fins due to the blockage effect induced by its choked cells. The reduction of the high drag associated with grid fins is also investigated by comparing the performances of two isolated grid fin geometries with and without the use of a Busemann biplane configuration. The application of this concept to grid fins reduces its drag in the supersonic regime while maintaining its beneficial lift characteristics. Furthermore, the drag of grid fins in transonic flow can be reduced by using an optimized profile with a higher inlet-to-throat area ratio.

## Nomenclature

$(C_{m_q} + C_{m_{\dot{\alpha}}})$	=	pitch-damping coefficient
$C_{m_y}$	=	pitching moment coefficient
$C_{m_{y,0}}$	=	static pitching moment coefficient
$C_{m_{\alpha}}$	=	static stability derivative
$C_p$	=	pressure coefficient
$C_{p,0}$	=	mean pressure coefficient
$C_{p,1}$	=	first harmonic component of the pressure coefficient
$C_{p,2}$	=	second harmonic component of the pressure coefficient
$D$	=	missile diameter, m
$F$	=	force, N
$k$	=	reduced frequency
$L$	=	missile length, m
$Ma$	=	Mach number
$N$	=	number of cycles in the pitching moment time history
$q$	=	pitching rate, rad/s
$Re$	=	Reynolds number
$S$	=	cross section of the missile at its maximum diameter, m <sup>2</sup>
$U_{\infty}$	=	freestream velocity, m/s
$y^+$	=	dimensionless wall distance
$\alpha$	=	angle of attack, deg

$\alpha_{\max}$	=	amplitude, deg
$\alpha_0$	=	mean angle of attack, deg
$\dot{\alpha}$	=	rate of change of angle of attack, rad/s
$\delta_c$	=	canard deflection angle, deg
$\phi$	=	phase, rad
$\omega$	=	angular velocity, rad/s

## I. Introduction

GRID fins, also commonly known as lattice fins, may be used in several application areas ranging from projectile/missile control surfaces [1–5] to space vehicle emergency brakes and stabilization devices [6,7]. In the application of missile control, lattice fins provide good maneuverability in the supersonic flow regime due to their ability to maintain lift at a high angle of attack and yield improved yaw and roll stability. The advantage of the short chord length of the lattice fin allows it to be easily folded along the missile body, resulting in a lower hinge moment. This reduces the size and weight of the actuator.

Grid fin aerodynamics has been investigated in the past by researchers, both experimentally and numerically, using different fin sizes, shapes [1,8], and grid patterns [9], and over a wide range of Mach numbers [3,4]. Washington and Miller [1] carried out wind-tunnel tests on 26 different grid fin models, varying their span, height, cell spacing, and web thickness at  $0.35 < Ma < 3.5$  and  $0 \text{ deg} < \alpha < 17 \text{ deg}$ . They reported the good supersonic control characteristics, the small variation of the center of pressure, and the small hinge moment induced by the use of grid fins. Simpson and Saddler [8] performed additional wind-tunnel tests at  $0.7 < Ma < 4.5$  and investigated the static stability of grid fins at a zero angle of attack, as well as their control effectiveness. They noted the significant role played by grid fins in the overall static stability, but also lower control effectiveness. Hiroshima and Tatsumi [9] conducted wind-tunnel experiments using square, triangular, and hexagonal grid patterns at  $0.5 < Ma < 2$  and  $-5 \text{ deg} < \alpha < 30 \text{ deg}$ . Their results showed little variation between the different shapes of the fin cells. DeSpirito and Sahu [3] and DeSpirito et al. [10,11] carried out viscous simulations of a grid fin missile with and without canards in the supersonic (at Mach numbers from 1.5 to 3), the transonic, and the subsonic regimes [12] ( $Ma = 0.6$  and  $0.9$ ). They reproduced successfully the static forces and moments obtained in

Presented as Paper 2014-3285 at the 32nd AIAA Applied Aerodynamics Conference, Atlanta, GA, 16–20 June 2014; received 20 October 2014; revision received 13 February 2015; accepted for publication 17 March 2015; published online 20 May 2015. Copyright © 2015 by Her Majesty the Queen in Right of Canada, as represented by the Minister of National Defence. Published by the American Institute of Aeronautics and Astronautics, Inc., with permission. Copies of this paper may be made for personal or internal use, on condition that the copier pay the \$10.00 per-copy fee to the Copyright Clearance Center, Inc., 222 Rosewood Drive, Danvers, MA 01923; include the code 1533-6794/15 and \$10.00 in correspondence with the CCC.

<sup>\*</sup>Research Associate; antoine.despeyroux@rmc.ca. Member AIAA (Corresponding Author).

<sup>†</sup>Graduate Student.

<sup>‡</sup>Undergraduate Student.

<sup>§</sup>Defence Scientist, Valcartier Research Centre.

wind-tunnel experiments, and they observed a reduced effect of canard vortices on grid fins compared to planar fins. They also reported an improved roll-control effectiveness in supersonic flow, whereas the roll effectiveness of the canards is decreased in transonic and subsonic regimes at  $\alpha > 2$  deg. A significant amount of data has been gathered on the static aerodynamic coefficients. Results on static stability derivatives have been presented in different works at a zero angle of attack. Dupuis and Berner [4] experimentally studied both a planar and a grid fin controlled missile at  $0.6 < Ma < 3$  and at  $-15 \text{ deg} < \alpha < 15 \text{ deg}$ . They noted that, unlike the planar fin missile, the grid fin controlled missile became statically unstable in subsonic flow, whereas its static stability increased with the Mach number. Abate et al. [13] performed ballistic range tests on a generic grid fin missile in the transonic flow regime ( $0.72 < Ma < 0.86$ ). They observed a rapid loss of stability at  $Ma \approx 0.8$ . Additional experiments on different geometric configurations of the grid fin showed that decreasing the web thickness or using fewer larger cells reduced the fin's drag. Wind-tunnel tests conducted by Fournier [5] on both grid fin and planar fin controlled missiles showed that the former configuration caused a significant reduction in static stability compared to the latter. Pruzan et al. [7] compared experimental results obtained for unswept and sweptback grid fins mounted on the Orion launch abort vehicle. They concluded that the use of swept grid fins improved the stability in pitch in comparison with unswept fins. The problem of dynamic stability derivatives for the lattice fin configuration has been addressed by fewer researchers. To the knowledge of the authors, only the experimental work of Dupuis et al. [14] includes pitch-damping derivatives (with roll-damping derivatives) for a grid fin projectile, at different supersonic Mach numbers and at zero incidence. The present study contributes to an improved understanding on the dynamic stability derivatives of lattice fin controlled devices.

One drawback of grid fins is that they exhibit a higher level of drag compared to conventional planar fins. This situation is particularly acute near the transonic regime due to the occurrence of choked flow in the cells forming the lattice structure [15]. As a matter of fact, the drag on grid fins can account for 50% of the total drag experienced by a missile with lattice fin control in the supersonic regime and up to 65% of the total drag in the transonic regime [16]. This problem has been discussed in a few previous studies. Schülein and Guyot [17] used wind-tunnel experiments with Euler simulations, in the high supersonic regime, on two grid fin geometries designed to reduce the wave drag. The leading edges of each cell of the grid fin are locally swept, leading to a decrease of the drag of nearly 40% compared to a nonswept lattice fin. Cai [18] proposed a sweptback grid fin design and performed viscous simulations showing a drag reduction of 13% over the range  $0.9 < Ma < 2$  relative to the baseline configuration. Zeng [16] carried out additional viscous simulations using sharpened leading edges on the sweptback grid fin. This configuration provided a drag reduction of 30% in the transonic regime and up to 50% in supersonic flow. The results obtained through these two studies were confirmed experimentally by Debiasi [19], who also showed that the characteristics of the sweptback grid fin were maintained at a nonzero angle of attack. In this study, we propose a different idea to alleviate the problem.

For vehicles in motion, static aerodynamic coefficients do not fully characterize the total imparted forces and moments. There are additional terms, known as dynamic derivatives, that account for the change in aerodynamic forces and moments due to body rate perturbations; they are therefore necessary to be able to accurately describe the airframe aerodynamic response [20]. Among these dynamic derivatives, pitch-damping derivatives, describing the attenuation of an oscillation in angle of attack with time, are of particular importance [21]. An efficient method to determine numerically the pitch-damping coefficient was introduced by Weinacht [21]. The method uses steady-state simulations of projectiles following a lunar coning motion [21–23]. However, this technique is limited to axisymmetric bodies at small angles of attack. In a more recent work, the forced oscillation method was successfully applied to the Basic Finner missile at different angles of attack [24,25]. It involves time-accurate simulations to calculate the pitch-damping derivatives.

Bhagwandin and Sahu [25] computed the pitch-damping coefficient for the Basic Finner missile at angles of attack up to 90 deg and found that their results exhibited little dependence on the grid density, the turbulence model, the time step, or inner iterations. A reduced frequency approach was also employed by Murman [24].

In the first part of the present work, we conduct in Sec. III a very detailed validation study on our unsteady Reynolds-averaged Navier–Stokes simulation (URANS) approach, presented in Sec. II, through comparisons of our URANS results with previously published experimental and numerical data in both the supersonic and transonic regimes. After the validation, we proceed to investigate the dynamic stability derivatives of lattice fin controlled devices in Sec. IV by considering the pitch-damping derivative in a grid fin missile using the forced oscillation method. Specifically, the URANS of a generic missile model [5,13] with either a conventional planar fin or a lattice fin tail control are carried out. The numerical results, expressed as pitch-damping coefficients along with static stability derivatives and aerodynamic force and moment coefficients, are evaluated in both the transonic and supersonic regimes, at different angles of attack up to 30 deg. In the third part of the present work, we present in Sec. V our studies on reducing the wave drag associated with lattice fins. We modify the lattice fin's geometry according to the Busemann biplane concept to take advantage of the “wave cancellation effect.” This approach borrows the idea from the work on silent and efficient supersonic airplanes of Kusunose et al. [26] and Hu et al. [27].

## II. Numerical Approach

### A. Numerical Determination of the Pitch-Damping Coefficient

The forced oscillation method consists of imposing on an airframe a sinusoidal planar pitching motion of amplitude  $\alpha_{\max}$  and angular velocity  $\omega$  about the missile's center of gravity at a given angle of attack  $\alpha_0$ :

$$\alpha(t) = \alpha_0 + \alpha_{\max} \sin(\omega t) \quad (1)$$

The unsteady pitching moment then depends on the angle of attack  $\alpha$ , the pitching rate  $q$ , and the rate of change of the angle of attack  $\dot{\alpha}$ . Assuming that the pitching moment is a linear function of these three parameters, it can be expressed, in the case of a planar pitching motion, as

$$C_{m_y}(t) = C_{m_{y,0}} + \frac{\partial C_{m_y}}{\partial \alpha} \alpha(t) + \frac{\partial C_{m_y}}{\partial (qD/2U_\infty)} \left( \frac{D}{2U_\infty} \right) q(t) + \frac{\partial C_{m_y}}{\partial (\dot{\alpha}D/2U_\infty)} \left( \frac{D}{2U_\infty} \right) \dot{\alpha}(t) \quad (2)$$

or

$$C_{m_y}(t) = C_{m_{y,0}} + C_{m_\alpha} \alpha(t) + C_{m_q} \left( \frac{D}{2U_\infty} \right) q(t) + C_{m_{\dot{\alpha}}} \left( \frac{D}{2U_\infty} \right) \dot{\alpha}(t) \quad (3)$$

where  $D$  is the missile diameter,  $U_\infty$  is the freestream velocity,  $C_{m_{y,0}}$  is the static pitching moment coefficient for the prescribed angle of attack  $\alpha_0$ ,  $C_{m_\alpha} = \partial C_{m_y} / \partial \alpha$  is the static stability derivative,

$$C_{m_q} = \partial C_{m_y} / \partial \left( \frac{qD}{2U_\infty} \right)$$

is the rate of change of the missile pitching moment coefficient  $C_{m_y}$  with the pitch rate  $q$  at a constant angle of attack  $\alpha_0$ , and

$$C_{m_{\dot{\alpha}}} = \partial C_{m_y} / \partial \left( \frac{\dot{\alpha}D}{2U_\infty} \right)$$

is the rate of change of the missile pitching moment with the rate of change of angle of attack at a constant pitch angle. Due to the

difficulty to extract each component individually, the pitch-damping coefficient is often expressed as the sum of both dynamic derivatives  $C_{m_q}$  and  $C_{m_{\dot{\alpha}}}$ . Note that, for a planar pitching motion,  $q = \dot{\alpha}$ . The pitch-damping coefficient and the static stability derivative  $C_{m_{\alpha}}$  can then be extracted from the time response of the pitching moment by computing the first Fourier coefficients of  $C_{m_y}(t)$ , as shown by Da Ronch et al. [28]:

$$(C_{m_q} + C_{m_{\dot{\alpha}}}) = \frac{2}{k\alpha_{\max}NT} \int_0^{NT} [C_{m_y}(t) - C_{m_{y,0}}] \cos(\omega t) dt \quad (4)$$

where  $N$  is the number of cycles,  $T = 2\pi/\omega$  is the period, and  $k = \omega D/2U_{\infty}$  is the reduced frequency.

Alternatively, the pitch-damping coefficient can be deduced from the difference between the maximum and minimum values of the moment coefficient at  $\alpha = \alpha_0$  during a pitchup/pitchdown cycle or from a linear regression technique, as used successfully by Bhagwandin and Sahu [25] and Da Ronch et al. [28].

### B. Numerical Methodology

All simulations are carried out using the finite volume Stanford University unstructured (SU<sup>2</sup>) [29] code on an unstructured mesh. The unsteady, compressible Reynolds-averaged Navier–Stokes (RANS) equations are solved employing a Jameson–Schmidt–Turbel (JST) second-order-accurate central-difference spatial discretization scheme [30] and the one-equation Spalart–Allmaras turbulence model [31]. A second-order dual-time formulation is applied to perform time integration.

The missile pitching motion is achieved through a rigid mesh motion where no relative motion occurs between grid nodes. Thus, the sinusoidal motion given in Eq. (1) is prescribed for the entire grid about the center of gravity (see Fig. 1). The grid motion is introduced in the conservation equations by means of an arbitrary Lagrangian–Eulerian formulation. Further details about the rigid mesh motion are given by Economou et al. [32].

Force coefficients are expressed as  $C_{\text{force}} = F/((1/2)\rho_{\infty}U_{\infty}^2S)$ , where  $S$  is the cross section of the missile at its maximum diameter. Moment coefficients are obtained from  $C_{\text{moment}} = M/((1/2)\rho_{\infty}U_{\infty}^2SD)$  with  $D$  as the missile maximum diameter.

### III. Code Validation

This section presents numerical results obtained with SU<sup>2</sup> on a panel of five test cases assessing the accurate modeling of flow features involved in grid fin missile flows. For each of these validation cases, experimental and numerical results are available in the literature for comparison. These five problems are divided into two categories: static and dynamic validations.

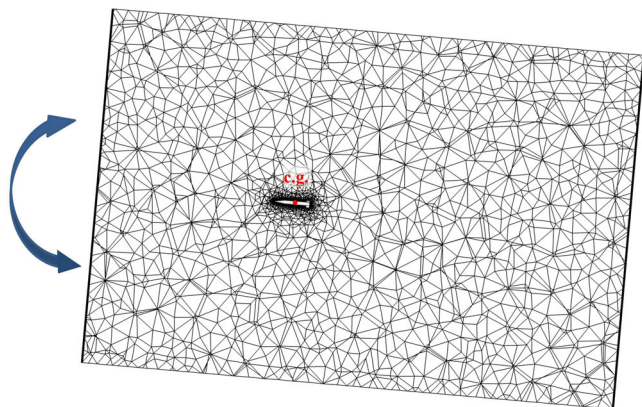


Fig. 1 Rigid mesh motion about the missile's center of gravity (c.g.).

### A. Static Validation

#### 1. Grid Fin Missile in Transonic Flow

As discussed in Sec. I, grid fin performance drops in transonic flow due to a complicated shock structure inside its lattice network. Furthermore, the appearance of a critical Mach number near 0.8 is shown by Abate et al. [13]. To assess the capability of SU<sup>2</sup> to accurately reproduce this complicated flowfield, steady-state simulations have been carried out on the test case investigated numerically by DeSpirito et al. [12] and for which experimental results have been obtained at Defence Research and Development Canada–Valcartier Research Centre [12]. This problem consists of studying a static canard-controlled missile with grid fins in cruciform configuration (see Fig. 2a), at a Mach number of  $Ma = 0.9$  and a Reynolds number of  $Re = 1.4 \times 10^7 \text{ m}^{-1}$ . Flight conditions and geometry details are given in Table 1. RANS equations are solved on an unstructured grid constituted of a prism-based boundary-layer mesh, ensuring a value of  $y^+ \approx 1$  in the vicinity of the missile boundary, immersed in tetrahedral cells (see Fig. 2a). Three meshes of 2, 4, and 10 million cells have been tested at a 2 deg angle of attack. The computed normal force differs by less than 1% between the medium and the fine grids. Far-field and nonreflective outflow boundary conditions are employed on the domain boundaries, whereas a no-slip/adiabatic wall condition is applied on the surface of the grid fin missile. The domain is a cylinder of length  $250D$  and a radius of  $50D$ , where  $D = 0.03 \text{ m}$  is the diameter of the missile. Results for the pitching moment coefficient, given here for the 4-million-cell grid, are in good agreement with experimental results and the numerical results obtained by DeSpirito et al. [12], as shown in Fig. 2b.

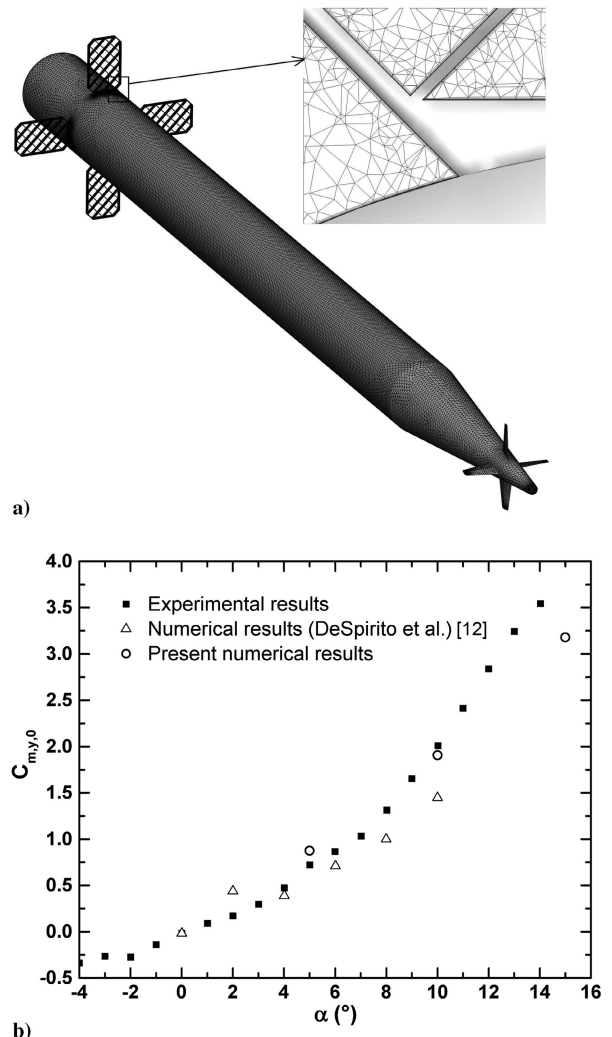


Fig. 2 Representations of a) geometry and mesh of the transonic grid fin missile, and b) pitching moment coefficient.

**Table 1** Flight conditions

Parameter	Value
$Ma$	0.9
$Re$	$1.4 \times 10^7 \text{ m}^{-1}$
$\alpha$	-4 to +15 deg
$\delta_c$	10 deg

## 2. Shock/Boundary-Layer Interaction on a Cylindrical Body

Shock/boundary-layer interaction plays an important role in flows around missiles, particularly when they involve grid fins. Thus, the Brosh and Kussoy [33] test case is used to assess the ability of the code to take into account the complex flowfield also encountered for lattice configurations featuring multiple separation zones, reflected shocks, and expansion fans. This experiment consists of a wedge immersed in a supersonic flow at  $Ma \approx 3$ , generating an oblique shock impinging a cylindrical surface. Detailed total and static pressure measurements in the cylindrical boundary layer are available.

RANS simulations are carried out on a structured hexahedral mesh (see Fig. 3), refined around the cylindrical wall where the non-dimensional wall distance is  $y^+ \approx 1$ . The domain, of dimensions  $1.35 \times 0.127 \times 0.1905 \text{ m}$ , is slightly longer than the one described in the experiment in the downstream region to improve numerical stability. Solutions have been obtained using the boundary conditions shown in Fig. 3, including a nonreflective outflow condition, no-slip/adiabatic wall conditions on the cylinder and the wedge, and a “supersonic inlet” boundary condition where all variables (temperature, static pressure, velocity vector) are specified at the inlet. Three grids of 2, 6, and 14 million cells have been compared. The computed pressure profiles normal to the cylindrical wall in the vicinity of the shock/boundary-layer interaction are similar for the medium and fine grids, whereas results for the coarse grid exhibit only a very small deviation from the other meshes. Results for the finest mesh are shown in this section. All solutions are obtained for the experimental flow conditions indicated in Table 2. The shock structure is illustrated in Figs. 4a to 4c, extracted from the symmetry plane of the domain. A “numerical schlieren” visualization is shown in Fig. 4a, whereas a comparison of experimental static pressure contours replotted from the data of Brosh and Kussoy [33] and numerical results are presented, respectively, in Figs. 4b and 4c. The global shock structure is, overall, well captured by the simulation. The 35 deg incident shock and the reflected shock are accurately predicted, whereas the same global patterns appear in both experimental and numerical results. The small high-pressure region at the root of the “separation shock” identified by Brosh and Kussoy is not reproduced by the simulation.

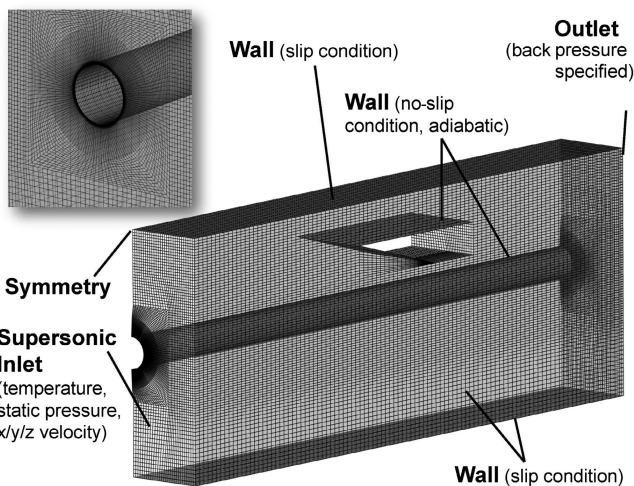


**Fig. 3** Boundary conditions and structured mesh used in  $SU^2$ , 10 times coarser than the grid discussed previously, for visualization purposes.

**Table 2** Experimental flow conditions used as input for the boundary conditions

Parameter	Value
$Ma$	2.85
$Re(10^6)$	18.2
Wedge angle $\alpha$	16 deg
Wedge position $h$	6.5 cm
$P_{t, \infty}$	25 psia
$T_{t, \infty}$	278 K

The pressure distribution on the windward ( $\Phi = 0$  deg) side of the cylinder is plotted in Fig. 5a. These results are in good agreement with experimental results from Brosh et al. [34]. The separation bubble is also accurately predicted, as confirmed by the representation of the pressure field on the cylinder in Fig. 5b. Experimental and computed pressure profiles in the boundary layer around the location of the shock/boundary-layer interaction are plotted in Figs. 6a and 6b. Simulations succeed in reproducing the global trend of the pressure profiles. However, some differences exist on the leeward side, which can be reduced by the use of a different turbulence model, such as Menter’s shear stress transport model [35].

## 3. Shock/Shock Interaction and Shock/Boundary-Layer Interaction in Hypersonic Flow

To investigate shock/shock and shock/boundary-layer interactions, Kussoy and Horstman [36] conducted experiments in the NASA Ames Research Center 3.5 ft hypersonic wind tunnel at  $Re = 5.3 \times 10^6 \text{ m}^{-1}$  and  $Ma = 8.3$ . A 76-cm-wide 220-cm-long

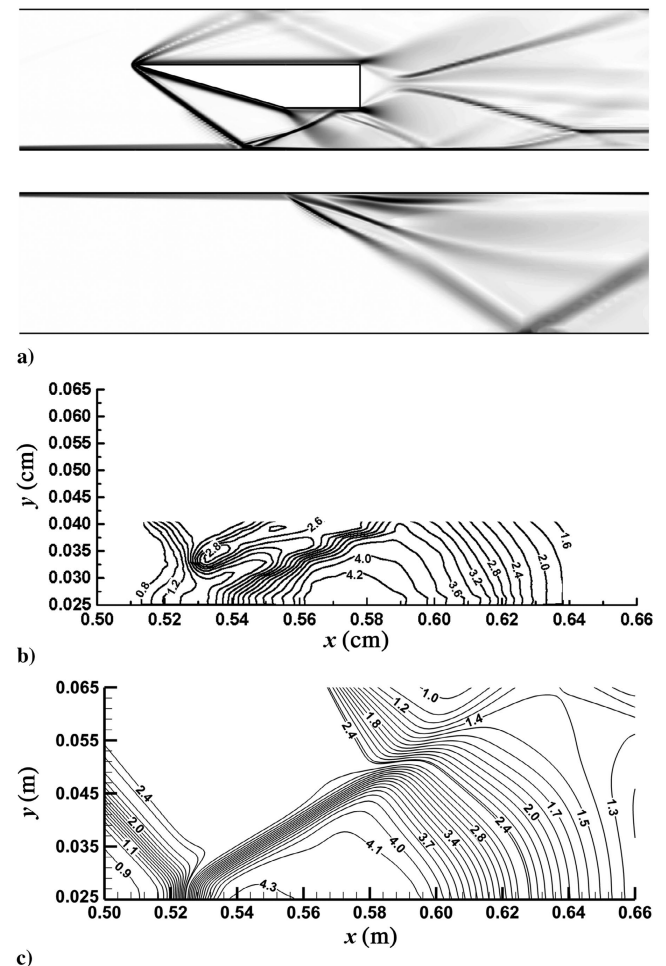


**Fig. 4** Representations of a) Schlieren like visualization of the shock structure in the symmetry plane (numerical results); b) experimental static pressure contours replotted from the data of Brosh and Kussoy [33]; and c) numerical static pressure contours in the symmetry plane.

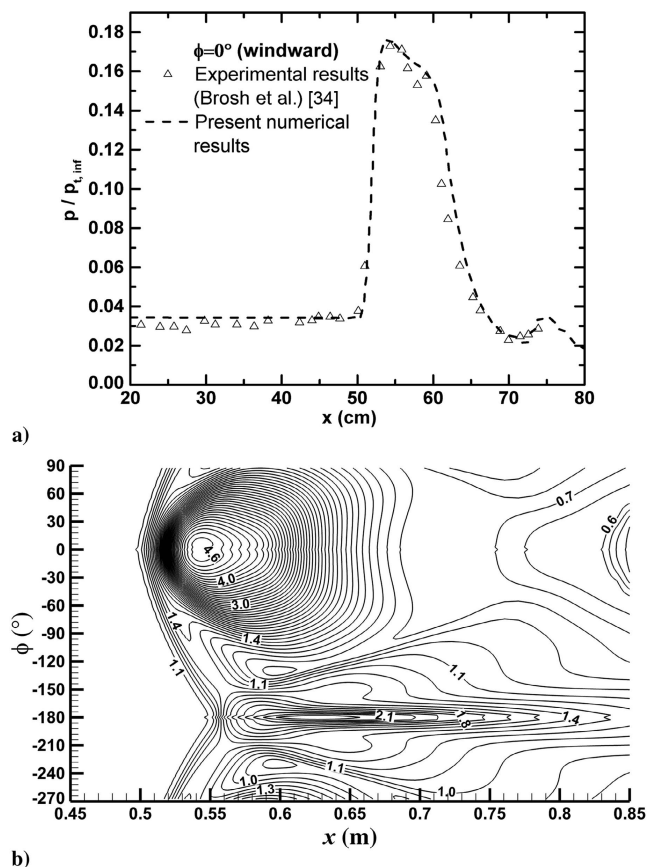


**Fig. 5** Representations of a) comparison between experimental results from Brosh et al. (1985) [34] and present numerical results for the pressure on the cylinder; b) surface pressure contours on the cylinder showing the separation bubble, in good agreement with experimental results obtained by Brosh et al. [34].

10-cm-thick water-cooled base plate was mounted in the test section, and it was maintained at a constant temperature of 300 K. The plate is set to a  $-2^\circ$  deg angle of attack, and its leading edge exhibits a 10 deg wedge shape. Two vertical wedge-shaped fins attached to the base plate allowed for a detailed study of the shock/shock interaction. Two pairs of fins with different wedge angles of 10 and 15 deg were tested.

This experiment thus constitutes an appropriate test case to check the ability of  $SU^2$  to capture shock/shock interactions such as those occurring inside or downstream the grid fin's cells. Three structured meshes of 0.75, 3, and 6 million hexahedral cells have been generated in a domain slightly longer than in the experiment, of dimensions  $3.2 \times 0.76 \times 0.45$  m. The amplitude of the predicted shock/shock interaction is similar in all three cases, and its location differs by approximately 1% between the medium and the fine mesh. In each case, the value of the first cell height adjacent to the plate's and fin's faces is set to ensure a value of  $y^+ \approx 1$ . RANS simulations are carried out using a nonreflective outflow condition; no-slip/isothermal wall conditions on the plate and fins; and a far-field boundary condition on the inlet, side, and top boundaries, where the freestream Mach number, Reynolds number, and temperature are specified. The boundary conditions and the mesh structure are shown in Fig. 7. The shock/shock and shock/boundary-layer interactions generated by the two fins are illustrated in Fig. 8a, where the shock structure is represented in the fin's midspan plane. Similar to the experimental observations, the stream traces are constricted by the passage and the increased pressure caused by the shock intersection results in the stream traces being diverted over the top of the splitter plate. Quantitatively, the pressure distribution on the plate along the centerline of the domain is presented for the medium mesh in Fig. 8b, along with Kussoy and Horstman's experimental results [36]. The difference between the computed and measured locations of the shock/shock interaction lies within 1%. The predicted amplitude of

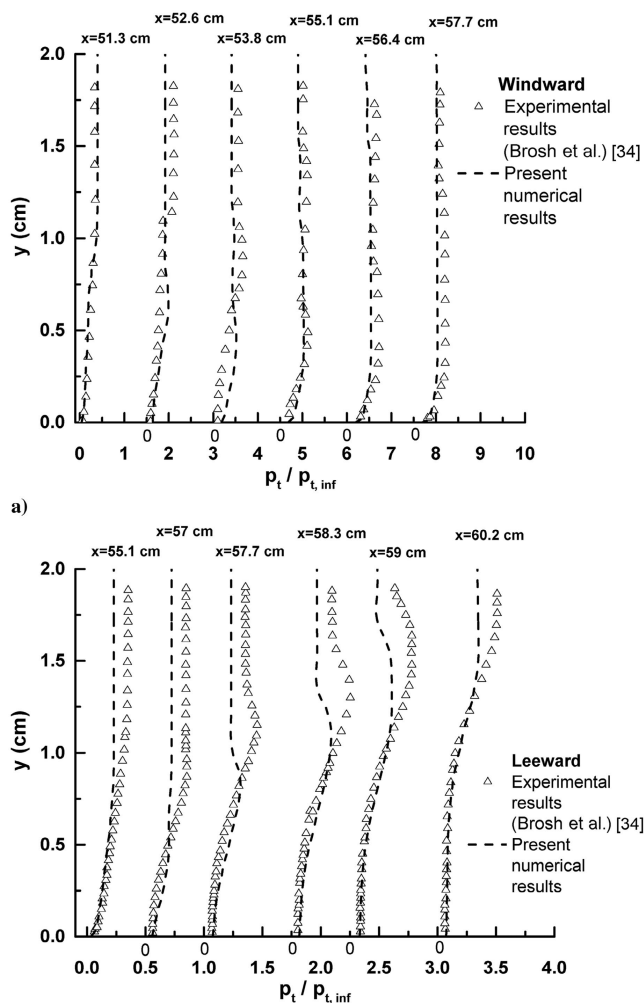


**Fig. 6** Profiles of total pressure normalized by its freestream value  $p_t / p_{t,\infty}$ , along the region of the cylinder where the shock/boundary-layer interaction occurs: a) windward side, and b) leeward side.

the pressure peak is found to be in fair agreement with experimental results, although underestimated.

## B. Dynamic Validation

### 1. Pitching Basic Finner Missile in Supersonic Flow

To check the rigid mesh motion method used in this work, the pitching Basic Finner missile is investigated, as it constitutes a standard test case for which various experimental and numerical

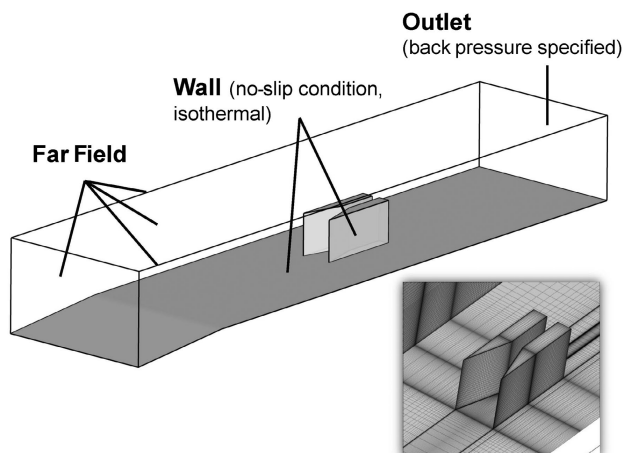


**Fig. 7** Computational domain and boundary conditions.

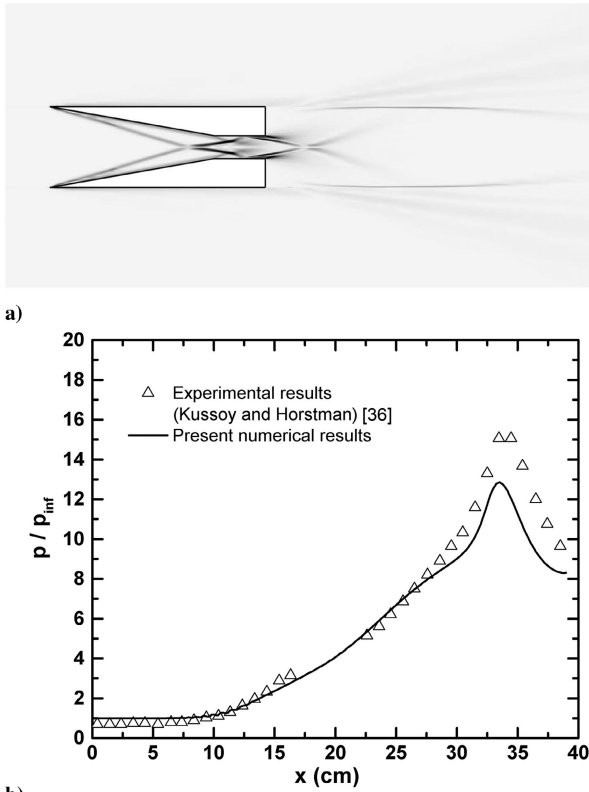


**Fig. 8** Representations of a) shock structure in a plane in the midspan of the wedges showing the shock/shock interaction; and b) pressure distribution on the plate along the centerline of the domain: the shock/shock interaction occurs at  $x \approx 0.34$  m.

results are available [24,25,37]. The problem consists of imposing a sinusoidal small-amplitude ( $\alpha_{max} = 1$  deg) pitching motion to the standard Basic Finner missile at a given frequency of 50 Hz in supersonic flow. This configuration, exhibiting a length-to-diameter ratio of  $L/D = 10$ , has been investigated experimentally by Usselton and Usselton [37] for angles of attack up to 90 deg. This work gave a basis to the numerical study of Murman [24], who used both a reduced frequency approach and time-accurate simulations with similar results at angles of attack up to 20 deg. Bhagwandin and Sahu [25] carried out time-dependent simulations with the same geometry to investigate high angles of attack up to 90 deg. The present study only concerns low to moderate angles of attack; the results of Usselton and Usselton [37] and Murman [24] are used to validate the rigid mesh motion capability of SU<sup>2</sup>. Flow conditions are given in Table 3.

RANS simulations are performed on an unstructured hybrid grid composed of a boundary-layer mesh with prisms in the vicinity of the missile wall and tetrahedral cells in the rest of the domain. The minimum wall distance is set to ensure a value of  $y^+$  close to one near the missile's surface. Three meshes of 1, 3, and 9 million cells have been compared with little difference between the two finest grids. Results will be presented, in this section, for the medium grid shown in Fig. 9. The domain is a cylinder of length  $150D$  and radius  $50D$ . Far-field and nonreflective outflow boundary conditions are used on the domain boundaries, whereas a no-slip/adiabatic wall condition is

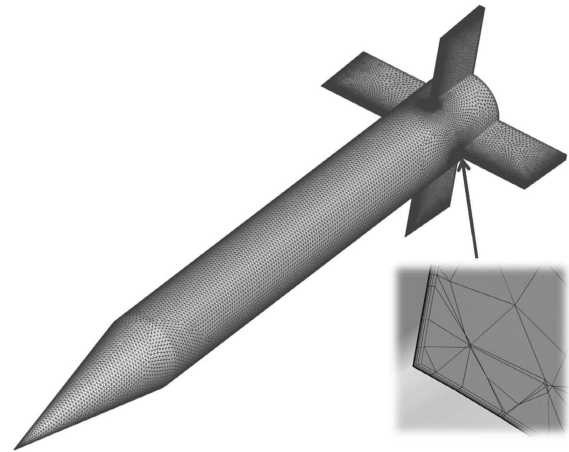


**Fig. 9** Detail of the mesh around the Basic Finner missile.

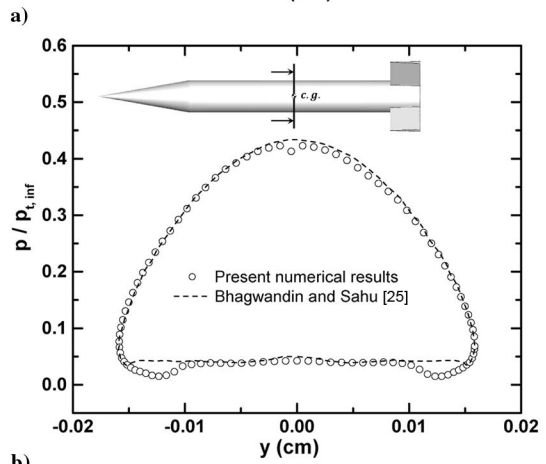
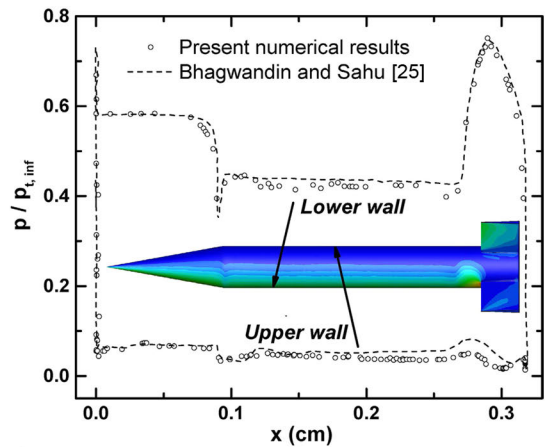


**Fig. 10** Pressure distribution on the missile: a) longitudinal plane, and b) transversal plane (at the location of the center of gravity).

**Table 3** Flow conditions for the pitching Basic Finner test case

Parameter	Value
$Ma$	1.96
$Re$	$0.086 \times 10^6$
$\alpha$	5 to 20 deg
$D$	0.031751 m
$L/D$	10

applied on the surface of the missile. The pitching motion is achieved by moving the entire domain, as described in Sec. II and shown in Fig. 1. The location of the center of gravity is recalled in Fig. 10. The time-step size is chosen as  $\Delta t = 2 \times 10^{-4}$  s, corresponding to 100 time steps per cycle. Values of 25 and 400 time steps per cycle have also been tested but had little effect on the solution, as long as enough inner iterations were specified for each time step to converge. In fact, the most important parameter was found to be the number of inner iterations, which should be at least 500 for the chosen value of 100 time steps per cycle. Values of the pitch-damping coefficient for 100, 500, and 1000 iterations per time step at  $\alpha = 20$  deg are presented in

Fig. 11c to illustrate their influence on the numerical results. All the values for the pitch-damping derivatives obtained in this section are calculated over the two last cycles in the time history of the pitching moment.

To validate the numerical model, steady-state simulations have first been carried out at a high angle of attack of  $\alpha = 45$  deg. The pressure distribution on the missile in both longitudinal and transversal planes (at the location of the center of gravity) is found to be in accordance with the numerical results obtained by Bhagwandin and Sahu [25], as seen in Figs. 10a and 10b.

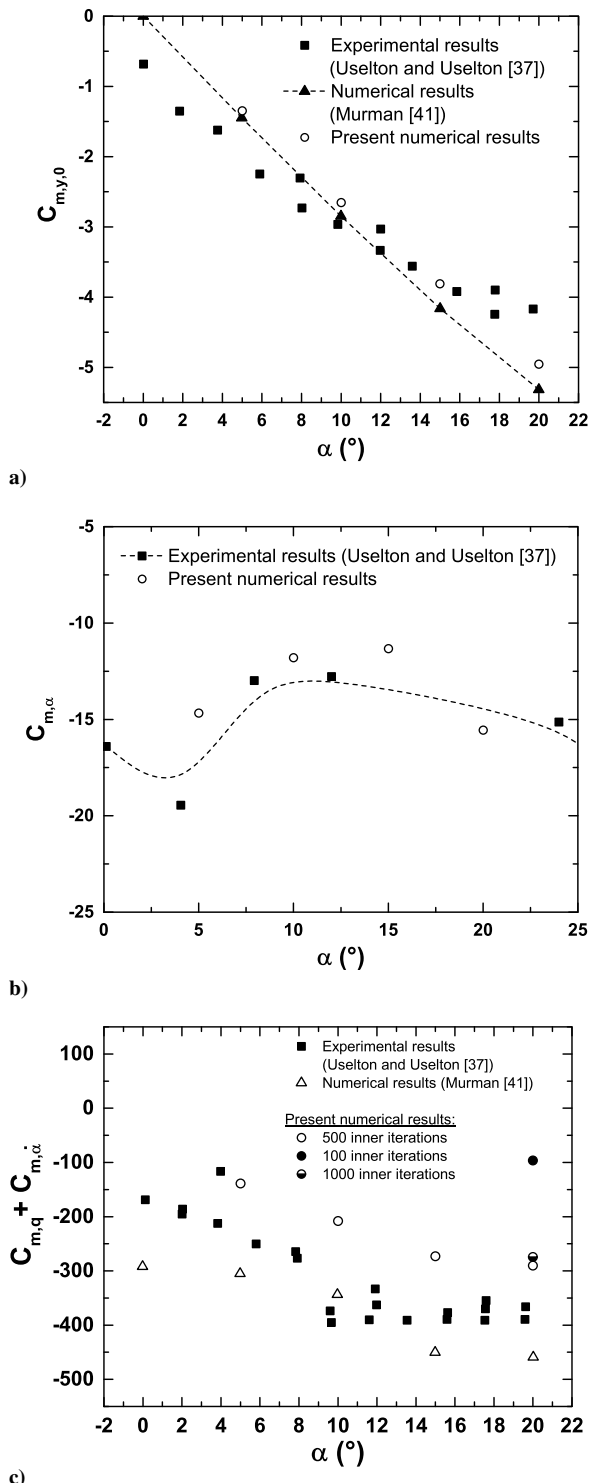


Fig. 11 Comparison of various experimental and numerical results: a) pitching moment coefficient  $C_{m,y,0}$ , b) static stability derivative  $C_{m,\alpha}$ , and c) dynamic stability derivative  $(C_{m,q} + C_{m,\alpha})$ .

Figures 11a, 11b, and 11c present, respectively, the static pitching moment coefficient  $C_{m,y,0}$ , the static stability derivative  $C_{m,\alpha}$ , and the pitch-damping coefficient  $(C_{m,q} + C_{m,\alpha})$ . The static moment coefficients and the values of the pitching moment slope  $C_{m,\alpha}$  are in good agreement with experimental and numerical results of Usselton and Usselton [37] and Murman [41]. A fair agreement is obtained for the computed pitch-damping coefficients, which succeed to reproduce the trend of experimental results, whereas their values differ slightly in the same range as numerical results obtained by Murman [24]. The larger errors related to the experimental determination of dynamic derivatives (estimated at  $\pm 20\%$  for the pitch-damping coefficient, according to DeSpirito et al. [23]), and the added difficulty to obtain accurate values at low reduced frequencies due to the thinning of the hysteresis curve [28], may explain such differences between numerical and experimental results.

2. Rolling Airframe Missile with Dithering Canards

A different dynamic configuration is employed to verify the ability of SU<sup>2</sup> to handle moving meshes. This case consists of a rolling airframe missile with dithering canards at  $Ma = 1.6$  and  $\alpha = 3$  deg, and it implies two rotating motions: a spinning movement at a spin rate of 8.75 Hz and a canard dither motion oscillating the canard deflection angle  $\delta_c$  between  $-15$  and  $+15$  deg, obeying a dither schedule, shown in Fig. 12a. The canards are moved following the sum of a command and dither signal, depending on the roll rate and the dither frequency. The amplitude of the command signal, or command level, is here fixed to zero. This case has been extensively studied over the last decade, and multiple numerical results using various computational fluid dynamics codes are available in the literature [38–43].

Then, in order to perform both roll and canard rotations, it is necessary to apply two distinct motions to the grid: the rolling motion must be imposed to all boundaries including the domain boundaries in order to avoid the grid deformation in the vicinity of the missile and outer boundaries (rotation of the fluid domain in block), whereas the

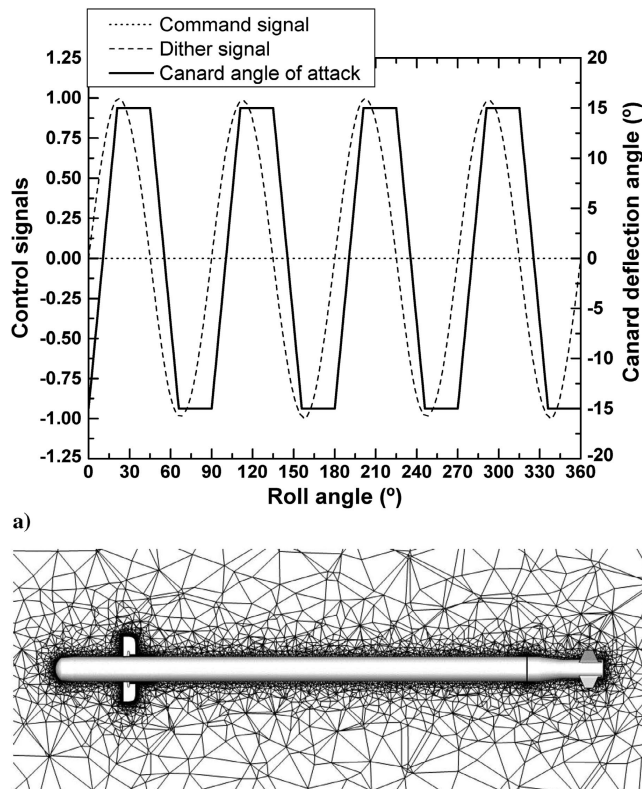
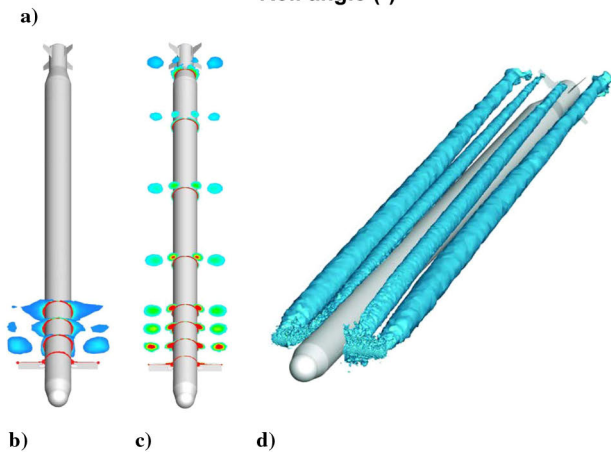
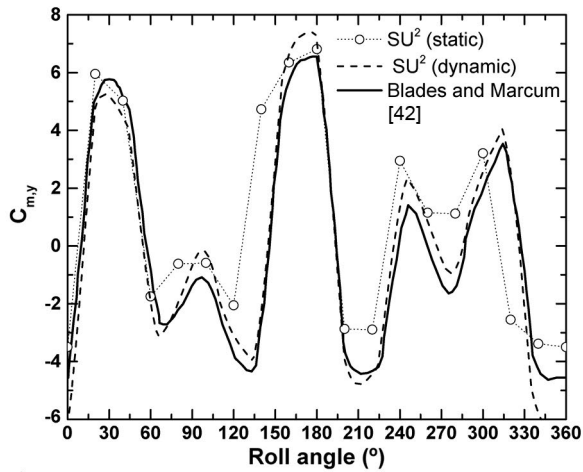


Fig. 12 Representations of a) canard dither scheme, and b) longitudinal section of the mesh.

canard motion is prescribed according to a command level of zero. Due to its complex nature, the latter is prescribed using given input files containing the updated coordinates of the nodes belonging to all boundaries at each time step. These files are generated before the computation through an external code reading boundary nodes information before performing both domain and canard rotations, accordingly, to the rolling and canard dither schemes. Numerical



**Fig. 13** Representations of a) pitching moment coefficient from static and dynamic simulations, as a function of the roll angle; and contours of helicity showing the accuracy of the canards vortices prediction for different sets of hybrid meshes/numerical schemes: b) 3 million cells/AUSM first order, c) 15 million cells/JST, and d) isosurface of helicity for the 15-million-cell mesh.

results using this approach have been obtained by solving Euler equations on unstructured, tetrahedral meshes in a cylindrical domain of length of  $300D$  and a radius of  $100D$ . The time-step size corresponds to a roll angle of  $1$  deg. A far-field boundary condition is used for the domain boundaries, whereas a wall boundary condition is applied on the missile's surface.

The pitching moment coefficient obtained with  $SU^2$  on a coarse grid of nearly 1 million cells (shown in Fig. 12b) is compared in Fig. 13 to the numerical results of Blades and Marcum [42], along with the coefficient obtained with  $SU^2$  from static configurations. Results on the pitching moment are in good agreement with the coefficients previously obtained by other authors. However, to be accurately captured, details of the flowfield such as canard horseshoe vortices need a higher grid resolution, as shown in Figs. 13b, 13c, and 13d.

#### IV. Pitch-Damping Prediction of Lattice Fin Configurations

The forced oscillation technique is applied on a generic missile of fineness equal to 16, similar to the model used by Abate et al. [13] and Fournier et al. [5], for which a few results on static aerodynamic coefficients as well as static stability derivatives are available. Planar fins exhibit a double-wedge profile, as described by DeSpirito et al. [11]. Details on the two geometries are given in Fig. 14. Both geometries are chosen such that the planar fin's projected area is approximately equal to the sum of the projected areas of the grid fin's webs. Both configurations also provide similar static stability around  $Ma = 2.5$ . Static stability in the high-Mach-number range is a criteria of particular interest for the comparison of agile missiles [8]. The static derivative  $C_{m_\alpha}$  is represented in Fig. 15 as a function of the Mach number. It can be seen that the grid fin configuration always has a lower static stability than the planar fin missile in the transonic and low supersonic regimes, whereas both configurations show similar values of  $C_{m_\alpha}$  in the high supersonic regime. A peak in transonic flow followed by a local minimum value of the static derivative can be noticed, which is a trend also observed by Abate et al. [13]. A cylindrical computational domain of length  $200D$  and radius  $50D$  is employed for all simulations. Three unstructured grids consisting of 2, 4, and 6 million cells have been studied, and little difference has been observed between the two finest meshes. Therefore, the 4-million-cell grid, consisting of mixed tetrahedral and prismatic elements in the boundary layer ( $y^+ \approx 1$ ), is used to compute all the results presented in this section (Fig. 16). Time-accurate simulations (URANS), following the procedure used for the Basic Finner validation case described previously (Sec. III), are carried out for both planar and lattice fin tail controls (in "+" configuration) in transonic ( $Ma = 0.9$ ) and supersonic regimes ( $Ma = 2$ ), for different angles of attack up to  $30$  deg, at a constant Reynolds number of  $Re \approx 10^6$ . A time-step size of  $\Delta t = 2.45 \times 10^{-4}$  s, corresponding to 100 time

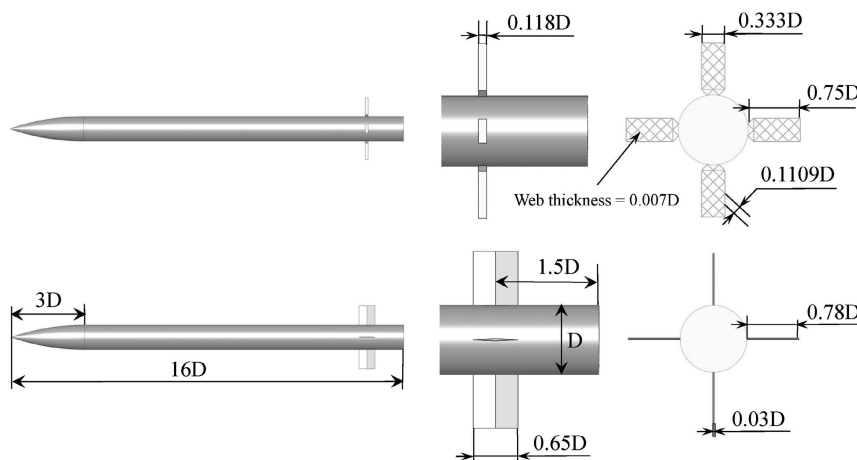


**Fig. 14** Geometry of the generic grid fin and planar fin controlled missiles used in this study.

steps per cycle, is employed in the simulations. Particular care has been taken in the influence of the number of inner iterations, as it has been found to be an important parameter in Sec. III. Values of 100, 500, and 1000 inner iterations have been tested using 100 time steps per cycle in the case of the grid fin missile at  $Ma = 2$  and  $\alpha = 0$  deg. The difference in the pitch-damping coefficient between 500 and 1000 inner iterations is less than 0.1%. Therefore, all calculations have been performed using 500 iterations per time step.

Only small-amplitude oscillations are considered in this study ( $\alpha_{max} = 0.5$  deg) and the reduced frequency is fixed to a value of  $k = \omega D / 2U_\infty = 0.05$ . Da Ronch et al. [28,44] showed that, at low and moderate angles of attack, the amplitude  $\alpha_{max}$  and the reduced frequency  $k$  do not have a significant influence on the pitch-damping coefficient. A study of the influence of  $k$  and  $\alpha_{max}$  on the solution for the present configuration confirmed this observation, as seen in Fig. 17 at  $Ma = 2$ . The evolution of the pitch-damping coefficient

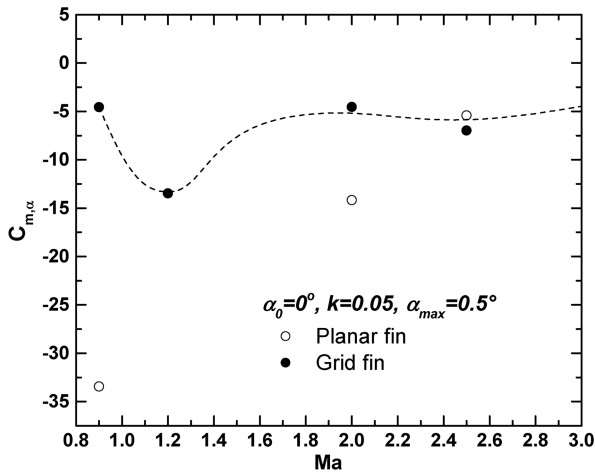


Fig. 15 Influence of the Mach number on the static stability of grid fin and planar fin configurations.

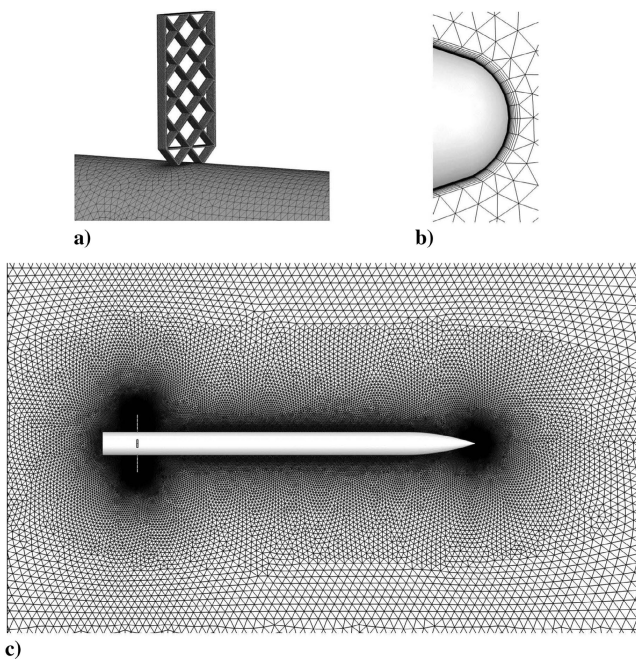


Fig. 16 Grid employed for the calculation of pitch-damping coefficients: a) detail of the mesh around grid fins, b) detail of the boundary layer mesh in the vicinity of the missile's nose, c) mesh structure in the symmetry plane.

with the amplitude in Fig. 17a exhibits a plateau for low values of  $\alpha_{max}$  and a sharp deviation for amplitudes approaching 1 deg in all configurations, following the dynamics of the body alone, plotted in the same figure. Figure 17b shows that  $(C_{m,q} + C_{m,i})$  has a similar behavior when the reduced frequency  $k$  is increased over 0.025. Thus, nonlinear effects induced by the body become significant for an amplitude of 1 deg at a reduced frequency  $k = 0.05$ , whereas this value is higher for lower frequencies. Although the presence of fins increases the dynamic stability of the missile in all cases, the planar fin controlled missile exhibits lower dynamic stability than the grid fin missile at low amplitudes and frequencies in supersonic flow. This lower value of the pitch-damping coefficient is consistent with the results of Dupuis et al. [14], who found a 30% lower value of  $(C_{m,q} + C_{m,i})$  for a grid fin projectile over the equivalent planar fin configuration.

Figures 18a and 18b depict typical time responses of the pitching moment  $C_{m,y}$  and hysteresis curves obtained for each angle of attack, respectively, at  $Ma = 2$  and  $Ma = 0.9$ . The initial perturbation, slightly visible in the hysteresis curve of Fig. 18a, disappears after half of the first cycle.

The pitch-damping coefficient at a zero angle of attack is presented in Fig. 19 for the grid fin configuration at different Mach numbers. This evolution exhibits a peak in transonic regime with a very low value of  $(C_{m,q} + C_{m,i})$ , indicating a loss in the missile's stability resulting from the choking occurring in the fins' cells, as has been observed by other researchers [5,13]. The pitch-damping coefficient is then slowly decaying in supersonic regime. It can be seen in the

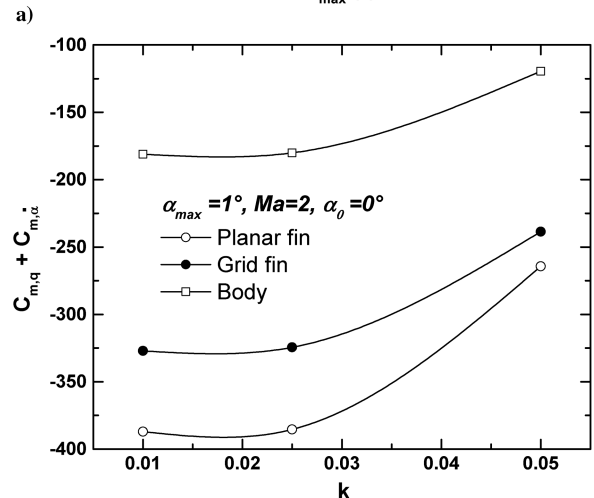
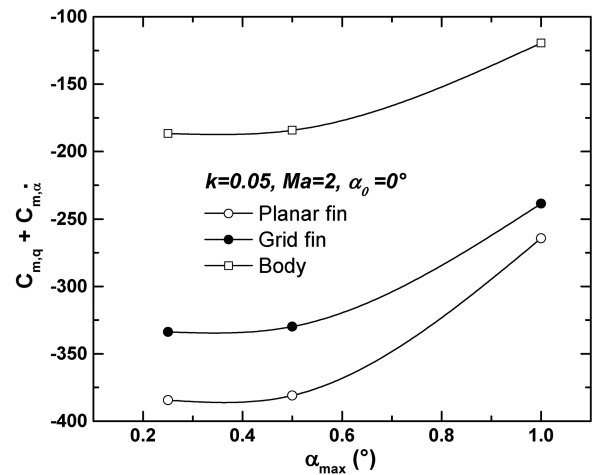
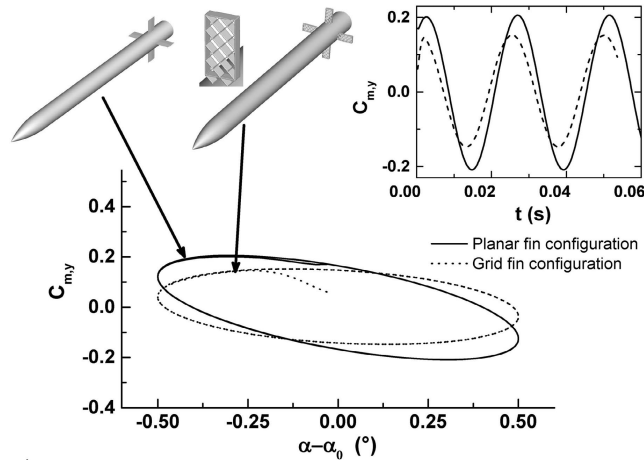
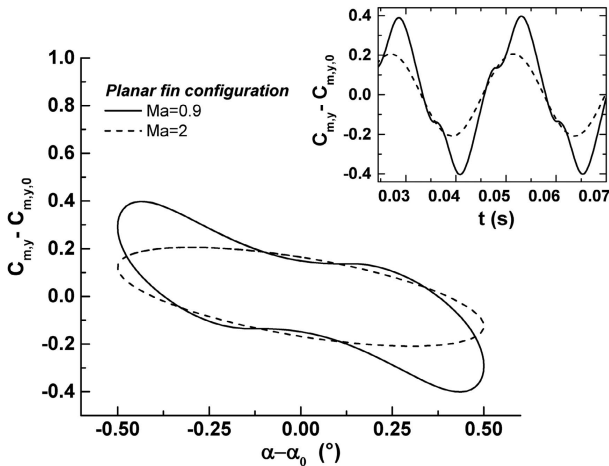


Fig. 17 Influence of the pitching motion's characteristics on the pitch-damping coefficient ( $Ma = 2, \alpha_0 = 0$  deg): a) influence of the amplitude  $\alpha_{max}$ , and b) influence of the reduced frequency  $k$ .



a)



b)

**Fig. 18** Representations of a) hysteresis curves showing the rapid damping of the initial perturbation for both grid fin and planar fin configurations at  $Ma = 2$  and  $\alpha = 0$  deg, and b) hysteresis curve for the planar fin configuration at  $Ma = 0.9$  and  $\alpha = 0$  deg. (Inserts show time history of  $C_{m_y}$ ).

same figure that the dynamic stability of the planar fin configuration is always higher than for the grid fin missile.

Results on the pitching moment coefficient  $C_{m_{y,0}}$ , the static derivative  $C_{m_\alpha}$ , and the pitch-damping sum ( $C_{m_q} + C_{m_\alpha}$ ) are, respectively, presented in Figs. 20a, 20b, and 20c in the supersonic regime and in Figs. 21a, 21b, and 21c in the transonic regime. The value of  $C_{m_\alpha}$  at a zero angle of attack is in good agreement with the experimental data obtained by Fournier et al. [5] and Abate et al. [13] for both Mach numbers.

At  $Ma = 2$ , it can be seen from Figs. 20b and 20c that the missile is statically and dynamically stable for the whole range of angles of attack  $\alpha$  considered in this study, due to the contribution of grid fins or planar fins. The moment experienced by grid fin and planar fin controlled missiles follows a similar evolution as  $\alpha$  increases, and it exhibits a change in its slope around  $\alpha = 15$  deg, as shown in Fig. 20b. The two configurations then undergo an increase in static stability at higher angles of attack. However, the center of pressure is always closer to the center of gravity for the grid fin missile than for the planar fin configuration, as has been found by other authors [5,13], although its location varies in a similar way with the angle of attack; thus, the lattice fin configuration provides a higher maneuverability. The pitch-damping derivative only shows a slight difference between grid fins and planar fins, as seen in Fig. 20c. Although both configurations contribute to the dynamic stability of the missile (Fig. 17), the pitch-damping moment does not seem to depend on the geometry of the tail fins. The general behavior of the pitch-damping sum, decreasing monotonically from  $\alpha = 0$  to 30 deg,

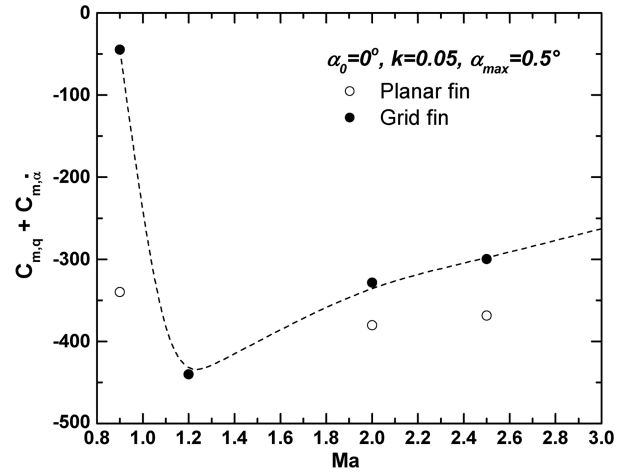


**Fig. 19** Evolution of the pitch-damping coefficient ( $C_{m_q} + C_{m_\alpha}$ ) with the Mach number.

and its high maximum absolute values are qualitatively consistent with wind-tunnel results obtained by Useltun and Useltun [37] for a missile of similar fineness in supersonic flow.

In transonic flow, at  $Ma = 0.9$ , the hysteresis curve followed by the pitching moment departs from its ellipsoidal shape (as seen in Fig. 18b) in all cases, due to the presence of nonlinear effects. Indeed, strong shock motions occur normal to the surfaces of planar fins approximately at midchord, similar to those observed for unsteady airfoils [45], as illustrated in Fig. 22b. Moreover, it is well known that the flow within the grid fin's cells is choked in this range of Mach numbers [15]. A shock motion is also observed in the lattice structure of grid fins, in the vicinity of the inlet and the outlet of the grid fin's cells, corresponding to the dark regions in the instantaneous contours of density gradient, shown in Fig. 22a. To understand how the flow around the pitching missile is affected in this nonlinear regime, the superposition method introduced by McCroskey [45] is employed on a planar fin and a grid fin element (along the midspan sections of a planar fin and one of the upper grid fin's cells). The pressure coefficient  $C_p$  is decomposed into its mean value and its first and second harmonics  $C_{p,1}$  and  $C_{p,2}$ , such as

$$C_p(t) = C_{p,0} + C_{p,1,Re} \cos(\omega t) + C_{p,1,Im} \sin(\omega t) + C_{p,2} \cos(2\omega t + \phi) \quad (5)$$

Figures 23a and 23b show how the pressure distribution on the planar fin and the grid fin element is altered by the pressure fluctuations induced by the motion of the shock waves. Peaks in  $C_{p,1}$  represent the pressure perturbations, which can reach a particularly large amplitude in the case of grid fins. The locations of these peaks are consistent with the locations of the shocks observed in Figs. 22a and 22b.

In the transonic regime, different behaviors of static and dynamic stability derivatives are observed for grid fin and planar fin controlled missiles. The static derivative  $C_{m_\alpha}$ , presented in Fig. 20b, exhibits low negative values at low angles of attack, as in supersonic flow, but then increase to slightly positive values at higher angles of attack due to the change in the slope of the pitching moment around  $\alpha = 20$  deg. Therefore, the grid fin configuration becomes statically unstable in the range of angles of attack comprised between 15 and 30 deg. On the contrary, the planar fin configuration remains statically stable at all angles of attack up to 30 deg, despite a smaller absolute value of  $C_{m_\alpha}$  at higher angles of attack compared to the supersonic regime. The pitch-damping derivative, plotted in Fig. 21c, seems to be more dependent on the fin configuration in transonic flow than in supersonic flow. The lattice fin configuration exhibits less damping in pitch than the planar fin missile. The pitch-damping sum becomes particularly low at a zero angle of attack, whereas it only experiences

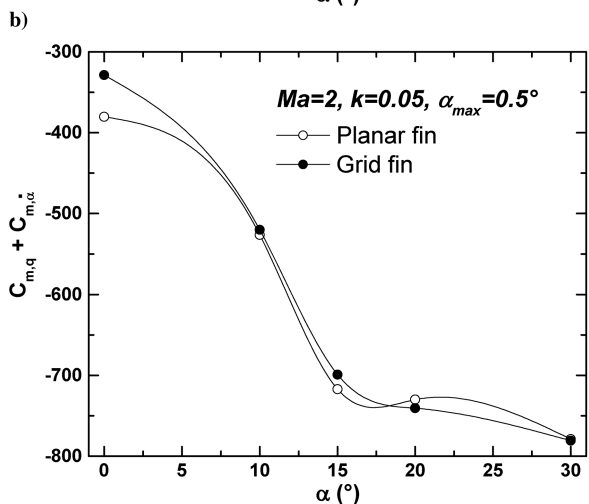
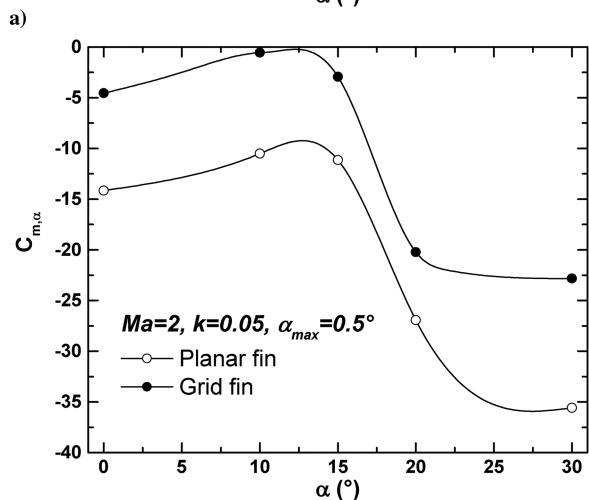
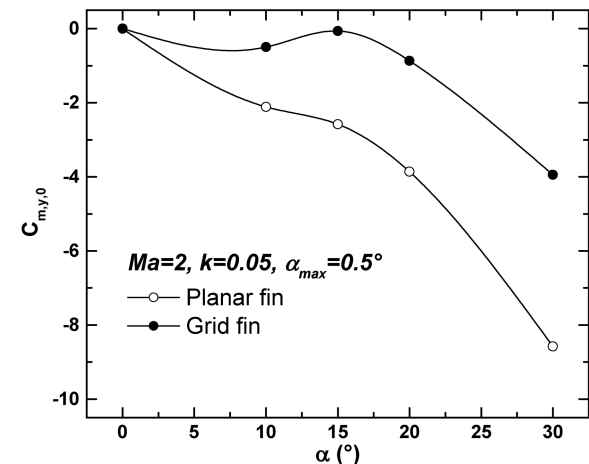


Fig. 20 Comparison between the pitching moments, static and dynamic derivatives obtained for planar fin and grid fin controlled missiles in the supersonic regime ( $Ma = 2$ ), for  $k = 0.05$  and  $\alpha_{max} = 0.5$  deg: a) pitching moment coefficient  $C_{m,y,0}$ , b) static stability derivative  $C_{m,\alpha}$ , and c) pitch-damping derivative ( $C_{m,q} + C_{m,\alpha}$ ).

a small decrease at higher angles of attack. The planar fin controlled missile experiences more damping than in supersonic flow, especially between  $\alpha = 20$  deg and  $\alpha = 30$  deg, where a sharp decrease in the dynamic derivative is observed. All cases remain dynamically stable for the whole range of angles of attack considered in this study.

The presence of shocks normal to planar fins affects both static and dynamic derivatives at low angles of attack. At higher values of  $\alpha$ , the

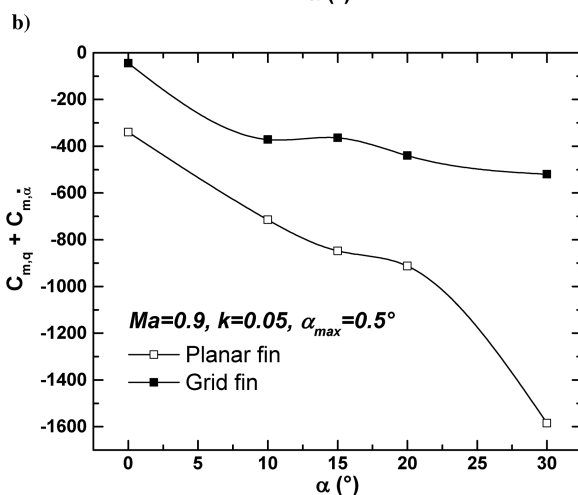
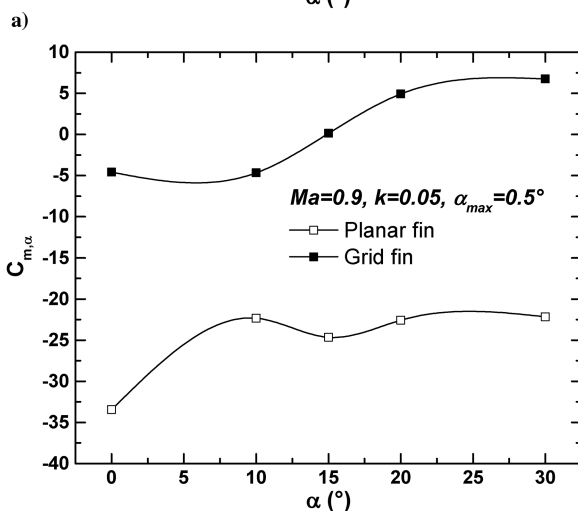
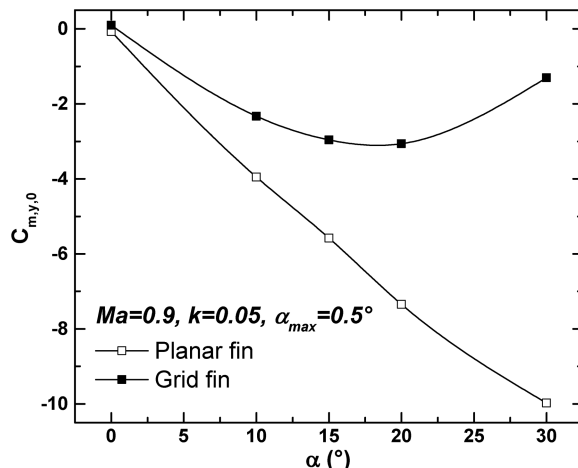
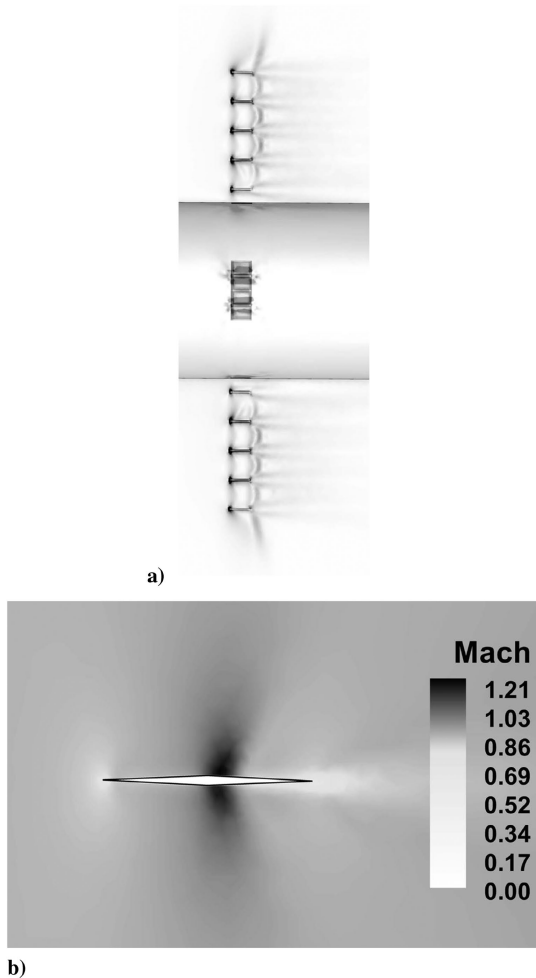


Fig. 21 Comparison between the pitching moments, static and dynamic derivatives obtained for planar fin and grid fin controlled missiles in the transonic regime ( $Ma = 0.9$ ), for  $k = 0.05$  and  $\alpha_{max} = 0.5$  deg: a) pitching moment coefficient  $C_{m,y,0}$ , b) static stability derivative  $C_{m,\alpha}$ , and c) pitch-damping derivative ( $C_{m,q} + C_{m,\alpha}$ ).

shock shifts to the fin's trailing edge while adopting a fishtail shape, as illustrated in Fig. 24b. The appearance of shocks inside the cells of the grid fin decreases the flow rate through it, reducing its lifting properties, which in turn attenuates its contribution to static and dynamic stability. Figure 24a shows that higher angles of attack amplify the shock structure in the grid fin's cells on the leeward side of the body, leading to static instability and reduced damping in pitch.



**Fig. 22 Shock structure around planar and grid fins in transonic flow at  $\alpha = 0$  deg: a) grid fin, and b) isovalues of the Mach number around a planar fin.**

## V. Drag Reduction Using the Busemann Biplane Concept

The high drag force generated by grid fins is one of the main problems limiting their use as control surfaces in missiles [15]. Few nonconventional designs have been proposed by other researchers to reduce wave drag using sweptback fins [7,16,46]. An alternative to the sweptback fin, investigated in this work, is based on the application of the Busemann biplane concept to grid fins. This concept consists of generating favorable wave interactions, at a specific Mach number, between two halves of a diamond airfoil of chord  $c$  separated by a distance  $0.5c$ . The internal flow between these two elements undergoes an isentropic compression across the compression waves generated at their leading edges. These waves vanish as they encounter each opposite profile oriented in the same direction as the flow. The undisturbed flow velocity and direction are recovered through an isentropic expansion [47]. Therefore, the aerodynamic forces produced by the flow between the two airfoil components are zero. The overall forces on the Busemann biplane reduce to those exerted by the external flow, i.e., the flow over a flat plate. In the actual flow, the presence of shock waves between the two half-diamond profiles generates entropy, leading to a higher wave drag. The application of the “wave cancellation” effect induced by this concept has been limited due to no lift generation of such configurations and the significantly high drag generated when operating outside design conditions [26,27]. Recent studies aimed at designing an efficient and silent supersonic airplane have made use of optimization methods to improve the performance of the Busemann biplane in a wider range of operating conditions [26,27]. Two

geometries are compared in this work: a simple “standard” grid fin of the same chord and thickness as the one studied in Sec. IV, and a “Busemann” grid fin of similar chord and average thickness. To assess the applicability of the Busemann biplane concept to grid fins, the Mach number at which the wave cancellation occurs is first chosen at  $Ma = 1.7$ , leading to a similar geometry to Kusunose et al. [26] and Hu et al. [27], given in Fig. 25. Euler simulations of the inviscid flow around single standard and Busemann grid fins have been carried out at a zero angle of attack and various Mach numbers using  $SU^2$ . To accurately capture the complex shock structure inside and around the grid fin, a structured mesh constituted of 2.5 million hexahedral elements was used for all calculations (Fig. 26a). This grid has been found to give similar results as two other grids of 0.7 and 6.75 million cells tested at  $Ma = 1.2$  (corresponding to a peak in the drag coefficient  $C_d$ ). To assess the contribution of viscous effects to the drag, RANS simulations have been performed for the Busemann grid fin at a zero angle of attack, using the Spalart–Allmaras model on an unstructured grid featuring a prism-based boundary-layer mesh (ensuring a value of  $y^+ \approx 1$  close to the fin) and tetrahedral cells in the rest of the domain. Three grids of 2.6, 5.3, and 9 million cells have been compared at  $Ma = 1.2$ . Although all the meshes produce values within a 1% difference from each other, the finest mesh (shown in Fig. 26b) is necessary to accurately capture the shock structure, which is particularly important to determine the onset of the wave cancellation effect at higher Mach numbers. Results for the drag coefficient for these two fins are presented in Fig. 27, along with experimental results obtained by other researchers for globally [16,19] and locally [46] sweptback grid fins with sharp leading edges. The evolution of the drag for the standard grid fin is in good agreement with the two experiments carried out by Debiasi [19] and Schulein and Guyot [46], whereas the drag of the Busemann grid fin is consistent with the two-dimensional numerical calculations performed by Hu et al. [27] on the original Busemann biplane geometry. The drag coefficient including viscous effects displays a similar behavior as in the inviscid case, except for a small increase in its value in the high supersonic regime. Although the drag is not decreased in the transonic regime due to the choking occurring in the cells in all cases, it is significantly reduced at higher Mach numbers for the Busemann grid fin, where a partial wave cancellation effect is observed. In the high supersonic regime, once shocks are completely swallowed through the cells, the evolution of the drag becomes similar to the diamond airfoil case, as observed by Kusunose et al. [26] and Hu et al. [27]. Although the globally sweptback grid fin performs better in the transonic regime, the Busemann grid fin provides a significantly lower drag in supersonic regime than all other configurations.

Figure 28 gives an illustration of the evolution of the shock structure at different Mach numbers: a normal shock forms at the trailing edge of the grid fin in transonic regime, as observed in the case of standard grid fins; and a bow shock arises ahead of the fin at low supersonic Mach numbers and remains until swallowed around the design Mach number. This shock structure explains the sharp increase in drag in transonic regime and the sudden drop in  $C_d$  at  $Ma > 1.7$ .

To understand how drag and lift are affected by the Busemann biplane geometry exhibited by the grid fin’s cells at a nonzero angle of attack, further Euler calculations have been carried out at  $\alpha = 10$  deg for different Mach numbers. The drag on standard and Busemann grid fins is shown in Fig. 29a. The wave cancellation phenomenon remains at  $\alpha \neq 0$  for the Busemann grid fin, although the Mach number at which it begins is seen to be slightly delayed due to the increasing difficulty to swallow the bow shock. The lift-to-drag ratio, presented in Fig. 29b, is significantly higher for the Busemann grid fin than in the case of the original fin at Mach numbers larger than the design point, and it remains equivalent to the standard grid fin in the transonic and low supersonic regimes. Therefore, performances in lift and drag seem to be conserved or improved when the angle of attack deviates from zero.

Then, the Busemann biplane geometry generates a high drag in the transonic and low supersonic regimes. Moreover, Kusunose et al. [26] and Hu et al. [27] have shown that the drag on such a con-

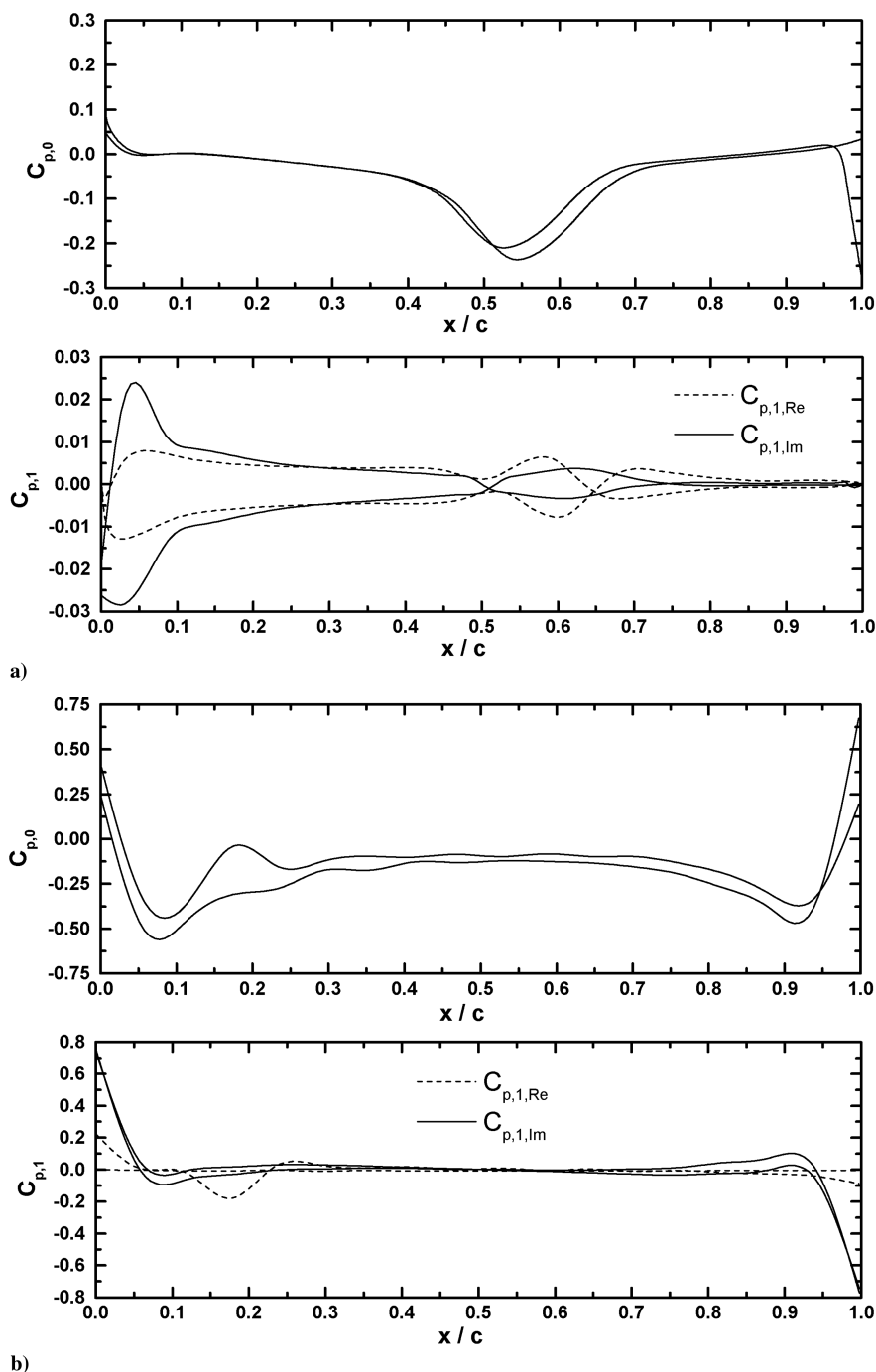


Fig. 23 Mean value  $C_{p,0}$  and first harmonic  $C_{p,1}$  of the pressure coefficient: a) around a planar fin, and b) around a grid fin element.

figuration exhibited different behaviors in situations of acceleration and deceleration, resulting in a flow-hysteresis effect. In this case, the Mach number at which the wave cancellation occurs is slightly higher for accelerations than for decelerations of the biplane. This phenomenon is highly dependent on the throat-to-inlet area ratio. Kusunose et al. [26] observed that the upper bound for the Mach number at which the Busemann effect takes place can be estimated by the Kantrowitz limit, delimiting the startable region of supersonic inlet diffusers. The lower bound can be approached by the isentropic contraction limit. To address these problems, Kusunose et al. [26] introduced slats and flaps in the two airfoil components to adjust the geometry to the flow regime, whereas Hu et al. [27] used an optimization method to improve the performances of the two-dimensional biplane at offdesign flow conditions. It is noticeable that the optimized geometry exhibits a higher inlet-to-throat area ratio,

thus reducing the range of Mach numbers in which the flow-hysteresis occurs.

This technique is applied to the Busemann grid fin to improve its performances in transonic regime. An “optimized Busemann” grid fin geometry is proposed in Fig. 30a, taking into account the main characteristics of the optimized Busemann biplane of Hu et al. [27]. The Mach number for which this configuration is designed is lowered to 1.6 in order to keep the same average thickness as the Busemann grid fin. The lattice network of the fin now alternates optimized Busemann sections and profiles close to the separated diamond configuration. Numerical results on the drag experienced by the optimized Busemann grid fin at a zero angle of attack have been obtained using Euler calculations in  $SU^2$ , and they are compared in Fig. 30b with the standard and baseline Busemann grid fins. The drag coefficient is reduced in transonic and low supersonic regimes in the

case of the optimized configuration, whereas it is slightly increased in the high supersonic regime. Hysteresis effects have not been investigated in this work but are also expected to be reduced. Figure 31 shows the details of the shock structure around the optimized Busemann grid fin at different Mach numbers.

Finally, the dynamic performances of isolated standard and Busemann grid fins are compared in Fig. 32 in transonic ( $Ma = 0.9$ )

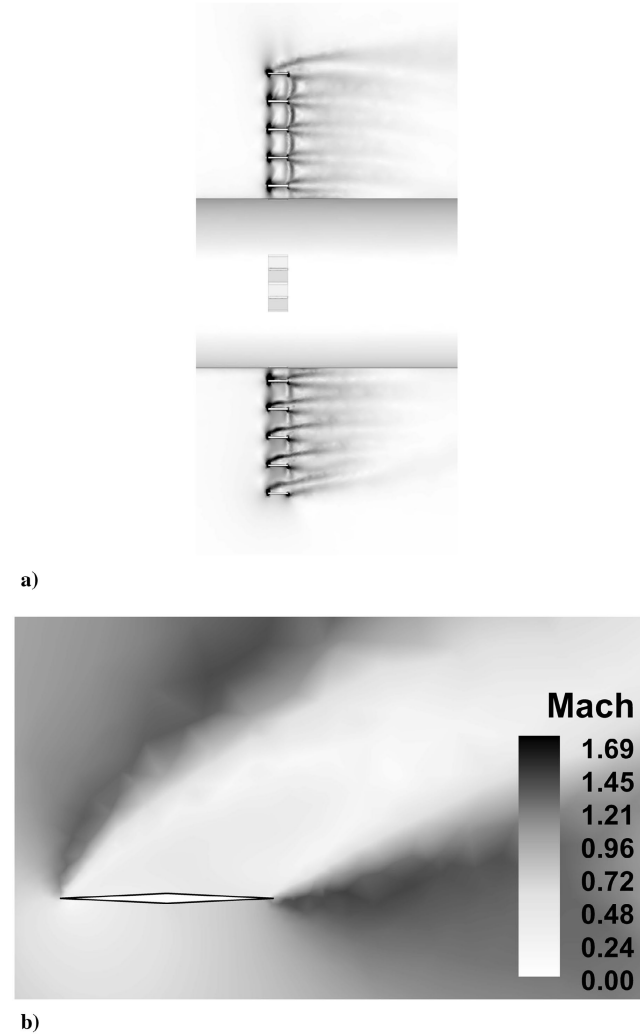


Fig. 24 Effect of the angle of attack on the shock structure around planar and grid fins in transonic flow (at  $\alpha = 30$  deg): a) grid fin, and b) isovalues of Mach number around a planar fin.

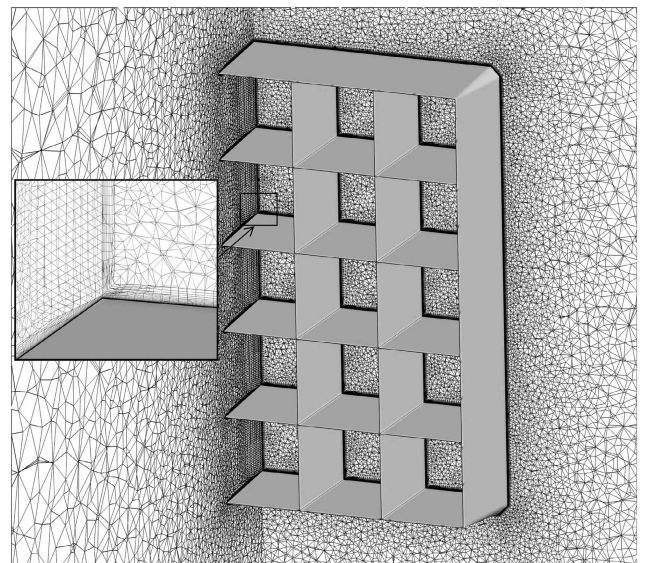
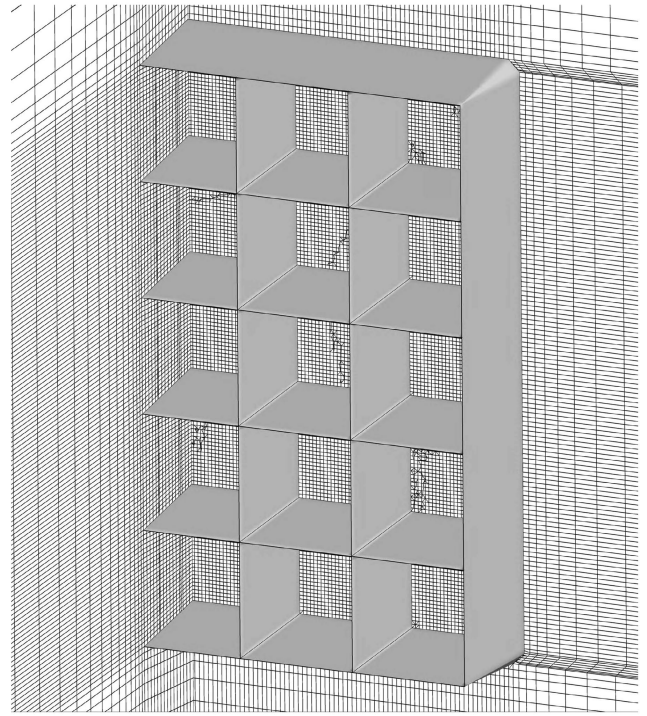


Fig. 26 Computational grid for the Busemann grid fin: a) Euler grid, and b) viscous grid.

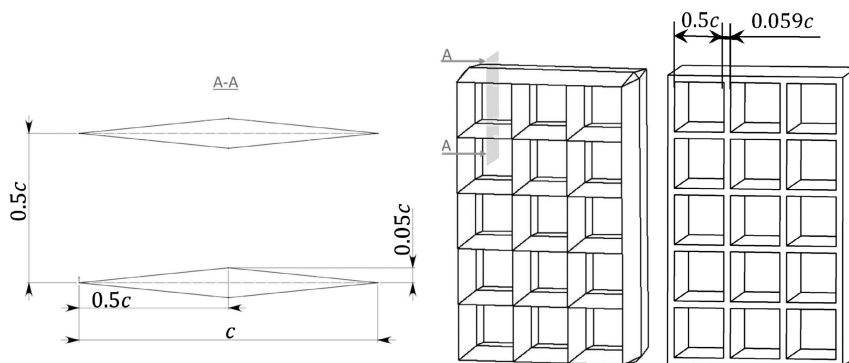


Fig. 25 Geometry of the Busemann grid fin compared to the standard grid fin.

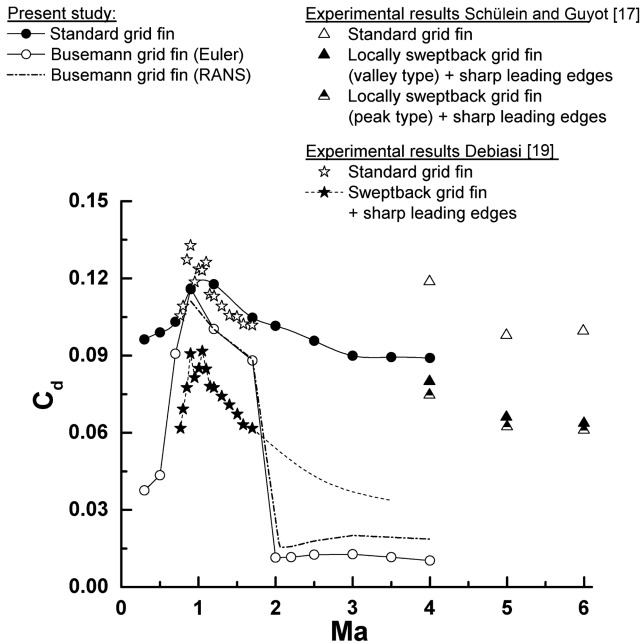


Fig. 27 Comparison of various experimental and numerical results on the drag coefficient of different grid fin designs with the present numerical results (Euler and RANS) on the Busemann grid fin, at a zero angle of attack. The dashed line corresponds to additional numerical results (RANS) obtained for the globally sweptback grid fin at high Mach numbers (validated at  $Ma = 1.7$ ) for comparison.

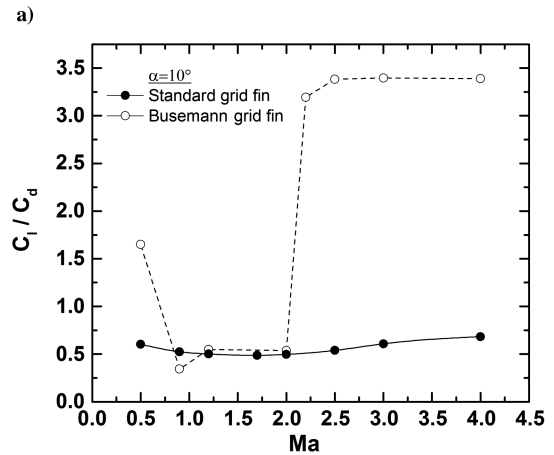
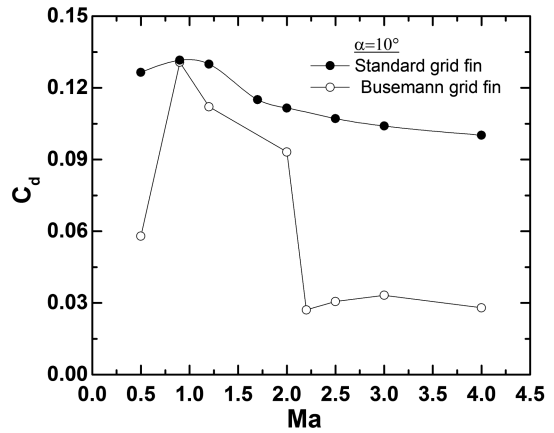


Fig. 29 Representations of a) drag coefficient of standard and Busemann grid fins at an angle of attack of  $\alpha = 10$  deg, and b) lift-to-drag ratio at  $\alpha = 10$  deg.

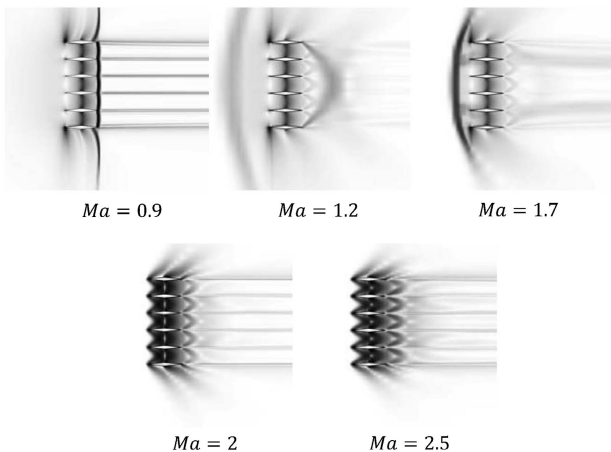


Fig. 28 Evolution of the shock structure around a Busemann grid fin at different Mach numbers.

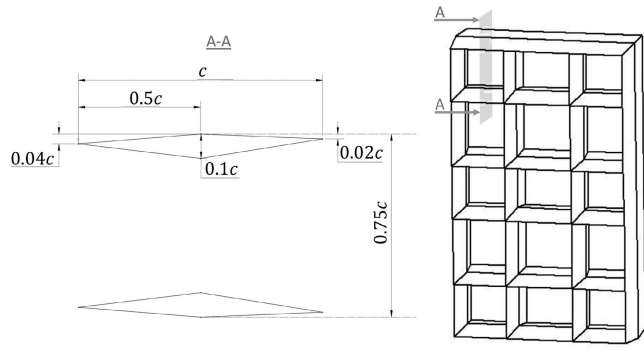
and supersonic ( $Ma = 2$ ) regimes. The pitch-damping coefficient is obtained using the same URANS method as used in Sec. IV with similar moment arm and pitching motion characteristics. Numerical results for the static and dynamic stability derivatives  $C_{m_{\alpha}}$  and  $(C_{m_q} + C_{m_{\dot{\alpha}}})$  are given in Table 4. Static stability properties seem to be conserved for the Busemann grid fin at all regimes. Dynamic stability properties are equivalent for both geometries in transonic flow, but a difference occurs in supersonic flow where the Busemann grid fin is seen to have reduced dynamic stability compared to the standard grid fin.

### VI. Conclusions

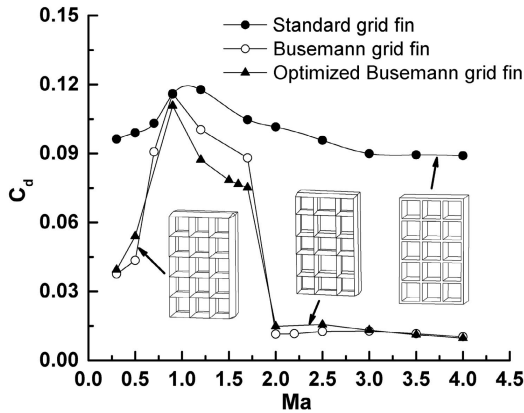
Static and dynamic performances of a grid fin controlled missile have been investigated with URANS for different flow regimes. A thorough validation study on the numerical approach has been

conducted. Pitch-damping dynamic derivatives have been obtained along with static stability derivatives and aerodynamic coefficients for a generic missile equipped with grid fins or planar fins, at angles of attack up to 30 deg in supersonic and transonic regimes. In all the cases, the grid fin configuration shows lower static stability. This implies that it has higher maneuverability than the planar fin tail control but becomes statically unstable at moderate angles of attack in the transonic regime. The dynamic derivative is shown to be independent from the types of fins in the supersonic regime. In the nonlinear transonic regime, planar fins are affected by the presence of moving shock waves normal to their surface at low angles of attack, which tend to disappear at higher incidence. The grid fin's cells are choked in transonic flow, leading to a blockage effect responsible for a loss in static and dynamic stability. The influence of shock waves is strengthened at high angles of attack. The use of grid fins on the generic missile provides less damping in pitch than in the case of the planar fin configuration in this flow regime for the whole range of angles of attack considered in this study. All configurations remain dynamically stable in both the supersonic and transonic regimes.

The problem of the high drag produced by the grid fin configuration has also been investigated. The application of the Busemann biplane concept to lattice fins significantly reduces the drag in the supersonic regime while maintaining the desirable lift characteristics. When the shock is completely swallowed in the grid fin's cells at high supersonic Mach numbers, although the drag does not benefit anymore from the wave cancellation effect, it still remains at a low level, as the flow is controlled by the diamond shape of the fin's wall section. The high drag in the transonic flow regime can be reduced by using an optimized Busemann profile having a higher inlet-to-throat area ratio. Most of the static and dynamic stability properties of the standard grid fin are conserved when changing the



a)



b)

**Fig. 30** Representations of a) geometry of an optimized Busemann grid fin; and b) comparison of the drag coefficient of standard, Busemann, and optimized Busemann grid fins at a zero angle of attack.

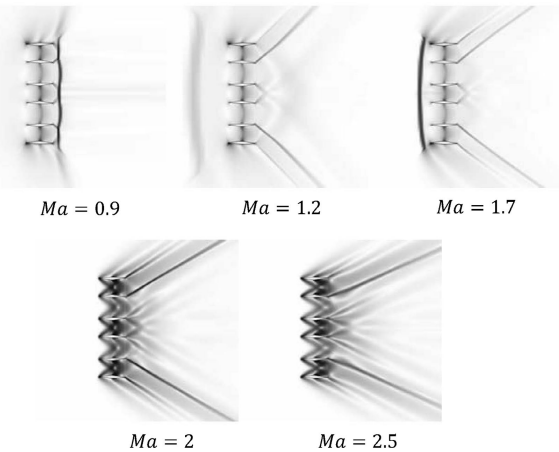


**Fig. 31** Evolution of the shock structure around an optimized Busemann grid fin at different Mach numbers.

**Table 4** Static and dynamic derivatives of pitching isolated standard and Busemann grid fins

Geometry	Mach number	$C_{m_\alpha}$	$(C_{m_\alpha} + C_{m_{\alpha'}})$
Standard grid fin	0.9	-1.28	-428.5
	2	-0.92	-239.5
Busemann grid fin	0.9	-1.23	-424.7
	2	-1.19	-142.6

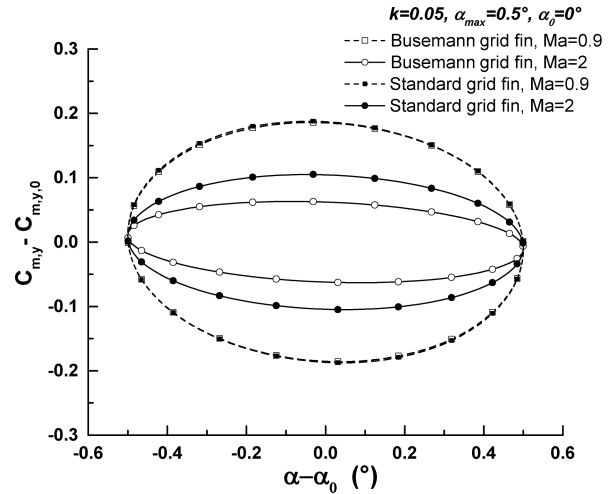


**Fig. 32** Hysteresis curves for pitching isolated standard and Busemann grid fins in transonic and supersonic regimes.

geometry to a Busemann grid fin, except in the supersonic regime where a decrease in dynamic stability is observed in the case of the new design.

**Acknowledgments**

Support from Defence Research and Development Canada – Valcartier Research Centre and the High Performance Computing Virtual Laboratory is acknowledged. The authors would like to thank Xiaohua Wu (Royal Military College of Canada) and François Lesage (Defence Research and Development Canada–Valcartier Research Centre) for their support of this work.

**References**

- [1] Washington, W. D., and Miller, M. S., “Experimental Investigations of Grid Fin Aerodynamics: A Synopsis of Nine Wind Tunnel and Three Flight Tests,” *Proceedings of RTO MP-5 Meeting on “Missile Aerodynamics”*, Research and Technology Organization, Neuilly-sur-Seine, France, 1998, pp. 10-1-10-14.
- [2] Chen, S., Khalid, M., Xu, H., and Lesage, F., “A Comprehensive CFD Investigation of Grid Fins as Efficient Control Surface Devices,” *38th Aerospace Sciences Meeting and Exhibit*, AIAA Paper 2000-0987, 2000.
- [3] DeSpirito, J., and Sahu, J., “Viscous CFD Calculations of Grid Fin Missile Aerodynamics in the Supersonic Flow Regime,” *39th Aerospace Sciences Meeting and Exhibit*, AIAA Paper 2001-0257, 2001.
- [4] Dupuis, A., and Berner, C., “Aerodynamic Aspects of a Grid Fined Projectile at Subsonic and Supersonic Velocities,” *19th International Symposium of Ballistics*, IBS 2001 Symposium Office, Thun, Switzerland, 2001, pp. 495-502.
- [5] Fournier, E. Y., “Wind Tunnel Investigation of a High L/D Projectile with Grid Fin and Conventional Planar Control Surfaces,” *19th International Symposium of Ballistics*, IBS 2001 Symposium Office, Thun, Switzerland, 2001, pp. 511-520.
- [6] Kless, J. E., and Aftosmis, M. J., “Analysis of Grid Fins for Launch Abort Vehicle Using a Cartesian Euler Solver,” *29th AIAA Applied Aerodynamics Conference*, AIAA Paper 2011-3666, 2011.
- [7] Pruzan, D., Mendenhall, M., Rose, W., and Schuster, D., “Grid Fin Stabilization of the Orion Launch Abort Vehicle,” *29th AIAA Applied Aerodynamics Conference*, AIAA Paper 2011-3018, 2011.
- [8] Simpson, G. M., and Sadler, A. J., “Lattice Controls: A Comparison with Conventional, Planar Fins,” *Proceedings of RTO MP-5 Meeting on “Missile Aerodynamics”*, Research and Technology Organization, Neuilly-sur-Seine, France, 1998, pp. 9-1-9-10.
- [9] Hiroshima, F., and Tatsumi, K., “Grid Pattern Effects on Aerodynamic Characteristics of Grid Fins,” *24th International Congress of the Aeronautical Sciences*, International Council of the Aeronautical Sciences (ICAS), Paper 092, Bonn, 2004.
- [10] DeSpirito, J., Edge, H. L., Weinacht, P., and Sahu, J., “Computational Fluid Dynamics Analysis of a Missile with Grid Fins,” *Journal of*

- Spacecraft and Rockets*, Vol. 38, No. 5, 2001, pp. 711–718.  
doi:10.2514/2.3756
- [11] DeSpirito, J., Jr., Vaughn, M. E., and Washington, W. D., “Numerical Investigation of Canard-Controlled Missile with Planar and Grid Fins,” *Journal of Spacecraft and Rockets*, Vol. 40, No. 3, 2003, pp. 363–370.  
doi:10.2514/2.3971
- [12] DeSpirito, J., Jr., Vaughn, M. E., and Washington, W. D., “Numerical Investigation of Aerodynamics of Canard-Controlled Missile Using Planar and Grid Tail Fins, Part II: Subsonic and Transonic Flow,” U.S. Air Force Research Lab., ARL-TR-3162, Wright-Patterson AFB, OH, 2004.
- [13] Abate, G., Winchenbach, G., and Hathaway, W., “Transonic Aerodynamic and Scaling Issues for Lattice Fin Projectiles Tested in a Ballistics Range,” *19th International Symposium of Ballistics*, IBS 2001 Symposium Office, Thun, Switzerland, 2001, pp. 413–420.
- [14] Dupuis, A., Berner, C., and Bernier, A., “Aerodynamic Characteristic of the A3 DRDCISL Reference Projectile: Missile with Lattice Fins,” Defence Research and Development Canada, Valcartier Research Centre TR-2005-216, Quebec City, QC, Canada, 2005.
- [15] Fleeman, E. L., *Tactical Missile Design*, AIAA, Reston, VA, 2001, pp. 40–42.
- [16] Zeng, Y., “Drag Reduction for Sweptback Grid Fin with Blunt and Sharp Leading Edges,” *Journal of Aircraft*, Vol. 49, No. 5, 2012, pp. 1526–1531.  
doi:10.2514/1.C031653
- [17] Schülein, E., and Guyot, D., “Novel High-Performance Grid Fins for Missile Control at High Speeds: Preliminary Numerical and Experimental Investigations,” *Proceedings of RTO-MP-AVT-135 Meeting on “Innovative Missile Systems”*, Research and Technology Organization, Neuilly-sur-Seine, France, 2006, pp. 35–1–35–28.
- [18] Cai, J., “Numerical Study on Choked Flow over Grid-Fin Configurations,” *Journal of Spacecraft and Rockets*, Vol. 46, No. 5, 2009, pp. 949–956.  
doi:10.2514/1.41442
- [19] Debiasi, M., “Measurements of the Forces and Moments Generated by Swept-Back Grid Fins,” *30th AIAA Applied Aerodynamics Conference*, AIAA Paper 2012-2909, 2012.
- [20] Nielsen, J. N., *Missile Aerodynamics*, McGraw-Hill, New York, 1988, pp. 349–431, Chap. 10.
- [21] Weinacht, P., “Prediction of Pitch-Damping for Symmetric Missiles,” *Proceedings of RTO MP-5 Meeting on “Missile Aerodynamics”*, Research and Technology Organization, Neuilly-sur-Seine, France, 1998, pp. 29-1–29-12.
- [22] Lesage, F., “Navier–Stokes Prediction of Pitch Damping Coefficients for Projectiles,” Defence Research and Development Canada, Valcartier Research Centre DREV-TM-9717, Quebec City, QC, Canada, 1997.
- [23] DeSpirito, J., Sifton, S. I., and Weinacht, P., “Navier–Stokes Predictions of Dynamic Stability Derivatives: Evaluation of Steady-State Methods,” *Journal of Spacecraft and Rockets*, Vol. 46, No. 6, 2009, pp. 1142–1154.  
doi:10.2514/1.38666
- [24] Murman, S. M., “Reduced-Frequency Approach for Calculating Dynamic Derivatives,” *AIAA Journal*, Vol. 45, No. 6, 2007, pp. 1161–1168.  
doi:10.2514/1.15758
- [25] Bhagwandin, V., and Sahu, J., “Numerical Prediction of Pitch Damping Stability Derivatives for Finned Projectiles,” *Journal of Spacecraft and Rockets*, Vol. 51, No. 5, 2014, pp. 1603–1618.  
doi:10.2514/1.A32734
- [26] Kusunose, K., Matsushima, K., and Maruyama, D., “Supersonic Biplane—A Review,” *Progress in Aerospace Sciences*, Vol. 47, No. 1, 2011, pp. 53–87.  
doi:10.1016/j.paerosci.2010.09.003
- [27] Hu, R., Jameson, A., and Wang, Q., “Adjoint-Based Aerodynamic Optimization of Supersonic Biplane Airfoils,” *Journal of Aircraft*, Vol. 49, No. 3, 2012, pp. 802–814.  
doi:10.2514/1.C031417
- [28] Da Ronch, A., Vallespin, D., Ghoreysi, M., and Badcock, K. J., “Evaluation of Dynamic Derivatives Using Computational Fluid Dynamics,” *AIAA Journal*, Vol. 50, No. 2, 2012, pp. 470–484.  
doi:10.2514/1.J051304
- [29] Palacios, F., Colonna, M. R., Aranake, A. C., Campos, A., Copeland, S. R., Economon, T. D., Lonkar, A. K., Lukaczyk, T. W., Taylor, T. W. R., and Alonso, J. J., “Stanford University Unstructured (SU2): An Open-Source Integrated Computational Environment for Multi-Physics Simulation and Design,” *51st AIAA Aerospace Sciences Meeting Including the New Horizons Forum and Aerospace Exposition*, AIAA Paper 2013-0287, 2013.
- [30] Jameson, A., Schmidt, W., and Turkel, E., “Numerical Solutions of the Euler Equations by Finite Volume Methods with Runge–Kutta Time Stepping Schemes,” *AIAA 14th Fluid and Plasma Dynamic Conference*, AIAA Paper 1981-1259, 1981.
- [31] Spalart, P., and Allmaras, S., “A One-Equation Turbulence Model for Aerodynamic Flows,” *30th Aerospace Sciences Meeting and Exhibit*, AIAA Paper 1992-0439, 1992.
- [32] Economon, T. D., Palacios, F., and Alonso, J. J., “Unsteady Aerodynamic Design on Unstructured Meshes with Sliding Interfaces,” *51st AIAA Aerospace Sciences Meeting Including the New Horizons Forum and Aerospace Exposition*, AIAA Paper 2013-0632, 2013.
- [33] Brosh, A., and Kussoy, M. I., “An Experimental Investigation of the Impingement of a Planar Shock Wave on an Axisymmetric Body at Mach 3,” NASA TM-84410, 1983.
- [34] Brosh, A., Kussoy, M. I., and Hung, C. M., “Experimental and Numerical Investigation of a Shock Wave Impingement on a Cylinder,” *AIAA Journal*, Vol. 23, No. 6, 1985, pp. 840–846.  
doi:10.2514/3.8996
- [35] Menter, F. R., “Zonal Two Equation  $k-\omega$  Turbulence Models for Aerodynamic Flows,” *24th Fluid Dynamics Conference*, AIAA Paper 1993-2906, 1993.
- [36] Kussoy, M. I., and Horstman, K. C., “Hypersonic Crossing Shock-Wave/Turbulent-Boundary-Layer Interactions,” *AIAA Journal*, Vol. 31, No. 12, 1993, pp. 2197–2203.  
doi:10.2514/3.11915
- [37] Usselton, B. L., and Usselton, J. C., “Test Mechanism for Measuring Pitch-Damping Derivatives of Missile Configurations at High Angles of Attack,” Arnold Engineering Development Center TR-AEDC-TR-75-43, Arnold AFB, TN, 1975.
- [38] Stalnaker, J. F., and Robinson, M. A., “Computation of Stability Derivatives of Spinning Missiles Using Unstructured Cartesian Meshes,” *20th AIAA Applied Aerodynamics Conference*, AIAA Paper 2002-2802, 2002.
- [39] Hall, L. H., “Chimera Moving Body Methodology for Rolling Airframe Missile Simulation with Dithering Canards,” *20th AIAA Applied Aerodynamics Conference*, AIAA Paper 2002-2801, 2002.
- [40] Nygaard, T. A., and Meakin, R. L., “Aerodynamic Analysis of a Spinning Missile with Dithering Canards,” *Journal of Spacecraft and Rockets*, Vol. 41, No. 5, 2004, pp. 726–734.  
doi:10.2514/1.13075
- [41] Murman, S. M., Aftosmis, M. J., and Berger, M. J., “Numerical Simulation of Rolling-Airframes Using a Multi-Level Cartesian Method,” *20th AIAA Applied Aerodynamics Conference*, AIAA Paper 2002-2798, 2002.
- [42] Blades, E. L., and Marcum, D. L., “Numerical Simulation of a Spinning Missile with Dithering Canards Using Unstructured Grids,” *Journal of Spacecraft and Rockets*, Vol. 41, No. 2, 2004, pp. 248–256.  
doi:10.2514/1.9197
- [43] Sheng, C., Wang, X., and Zhao, Q., “Aerodynamic Analysis of a Spinning Missile Using a High Order Unstructured-Grid Scheme,” *Journal of Spacecraft and Rockets*, Vol. 47, No. 1, 2010, pp. 81–89.  
doi:10.2514/1.42988
- [44] Ronch, A. D., McCracken, A. J., Badcock, K. J., Widhalm, M., and Campobasso, M. S., “Linear Frequency Domain and Harmonic Balance Predictions of Dynamic Derivatives,” *Journal of Aircraft*, Vol. 50, No. 3, 2013, pp. 694–707.  
doi:10.2514/1.C031674
- [45] McCroskey, W. J., “Unsteady Airfoils,” *Annual Review of Fluid Mechanics*, Vol. 14, Jan. 1982, pp. 285–311.  
doi:10.1146/annurev.fl.14.010182.001441
- [46] Schülein, E., and Guyot, D., “Wave Drag Reduction Approach for Lattice Wings at High Speeds,” *New Results in Numerical and Experimental Fluid Mechanics VI*, Vol. 96, edited by Tropea, C., Jakirlic, S., Heinemann, H.-J., Henke, R., and Hönlinger, H., Springer-Verlag, Berlin, 2008, pp. 332–339.
- [47] Ferri, A., *Elements of Aerodynamics of Supersonic Flows*, Macmillan Co., New York, 1949, pp. 154–160.

M. Miller  
Associate Editor

<b>DOCUMENT CONTROL DATA</b>		
(Security markings for the title, abstract and indexing annotation must be entered when the document is Classified or Designated)		
1. ORIGINATOR (The name and address of the organization preparing the document. Organizations for whom the document was prepared, e.g., Centre sponsoring a contractor's report, or tasking agency, are entered in Section 8.)  <b>DRDC – Valcartier Research Centre            Defence Research and Development Canada            2459 route de la Bravoure            Quebec (Quebec) G3J 1X5            Canada</b>	2a. SECURITY MARKING (Overall security marking of the document including special supplemental markings if applicable.)  <b>CAN UNCLASSIFIED</b>	
	2b. CONTROLLED GOODS  <b>NON-CONTROLLED GOODS            DMC A</b>	
3. TITLE (The complete document title as indicated on the title page. Its classification should be indicated by the appropriate abbreviation (S, C or U) in parentheses after the title.)  <b>Numerical Analysis of Static and Dynamic Performances of Grid Fin Controlled Missiles</b>		
4. AUTHORS (last name, followed by initials – ranks, titles, etc., not to be used)  <b>Despeyroux, A.; Hickey, J.P.; Desaulnier,R.; Luciano, R.; Piotrowski, M.; Hamel, N.</b>		
5. DATE OF PUBLICATION (Month and year of publication of document.)  <b>December 2017</b>	6a. NO. OF PAGES (Total containing information, including Annexes, Appendices, etc.)  <b>17</b>	6b. NO. OF REFS (Total cited in document.)  <b>47</b>
7. DESCRIPTIVE NOTES (The category of the document, e.g., technical report, technical note or memorandum. If appropriate, enter the type of report, e.g., interim, progress, summary, annual or final. Give the inclusive dates when a specific reporting period is covered.)  <b>External Literature (P)</b>		
8. SPONSORING ACTIVITY (The name of the department project office or laboratory sponsoring the research and development – include address.)  <b>DRDC – Valcartier Research Centre            Defence Research and Development Canada            2459 route de la Bravoure            Quebec (Quebec) G3J 1X5            Canada</b>		
9a. PROJECT OR GRANT NO. (If appropriate, the applicable research and development project or grant number under which the document was written. Please specify whether project or grant.)	9b. CONTRACT NO. (If appropriate, the applicable number under which the document was written.)	
10a. ORIGINATOR'S DOCUMENT NUMBER (The official document number by which the document is identified by the originating activity. This number must be unique to this document.)  <b>DRDC-RDDC-2017-P134</b>	10b. OTHER DOCUMENT NO(s). (Any other numbers which may be assigned this document either by the originator or by the sponsor.)	
11a. FUTURE DISTRIBUTION (Any limitations on further dissemination of the document, other than those imposed by security classification.)  <b>Public release</b>		
11b. FUTURE DISTRIBUTION OUTSIDE CANADA (Any limitations on further dissemination of the document, other than those imposed by security classification.)		

12. **ABSTRACT** (A brief and factual summary of the document. It may also appear elsewhere in the body of the document itself. It is highly desirable that the abstract of classified documents be unclassified. Each paragraph of the abstract shall begin with an indication of the security classification of the information in the paragraph (unless the document itself is unclassified) represented as (S), (C), (R), or (U). It is not necessary to include here abstracts in both official languages unless the text is bilingual.)

Grid fins provide good maneuverability to missiles in supersonic flow because they can maintain lift at a higher angle of attack. Although static aerodynamic data exist, very little quantitative dynamic performance information is available for grid fin controlled missiles. The high drag associated with grid fins is also a concern. Dynamic simulations are carried out using computational fluid dynamics to investigate the dynamic stability of a generic missile, controlled by grid fins or planar fins, in supersonic and transonic regimes at angles of attack up to 30 deg. In supersonic flow, the pitch-damping derivative is found to be insensitive to the control fin type; however, in transonic flow, grid fins provide a lower damping in pitch than planar fins due to the blockage effect induced by its choked cells. The reduction of the high drag associated with grid fins is also investigated by comparing the performances of two isolated grid fin geometries with and without the use of a Busemann biplane configuration. The application of this concept to grid fins reduces its drag in the supersonic regime while maintaining its beneficial lift characteristics. Furthermore, the drag of grid fins in transonic flow can be reduced by using an optimized profile with a higher inlet-to-throat area ratio.

---

13. **KEYWORDS, DESCRIPTORS or IDENTIFIERS** (Technically meaningful terms or short phrases that characterize a document and could be helpful in cataloguing the document. They should be selected so that no security classification is required. Identifiers, such as equipment model designation, trade name, military project code name, geographic location may also be included. If possible keywords should be selected from a published thesaurus, e.g., Thesaurus of Engineering and Scientific Terms (TEST) and that thesaurus identified. If it is not possible to select indexing terms which are Unclassified, the classification of each should be indicated as with the title.)

missile; CFD; Aerodynamic; grid fin